HHS Public Access

Author manuscript

Nat Immunol. Author manuscript; available in PMC 2022 November 26.

Published in final edited form as:

Nat Immunol. 2022 June ; 23(6): 868–877. doi:10.1038/s41590-022-01210-5.

Autoreactive CD8+ T cells are restrained by an exhaustion-like program that is maintained by LAG3

Stephanie Grebinoski[1,2,3,&], **Qianxia Zhang**[1,2,3,12,&], **Anthony R Cillo**[1,3], **Sasikanth Manne**[4,5], **Hanxi Xiao**[6,7], **Erin A. Brunazzi**[1,3], **Tracy Tabib**[8], **Carly Cardello**[1,3], **Christine G. Lian**[9], **George F. Murphy**[9], **Robert Lafyatis**[8], **E. John Wherry**[4,5,10], **Jishnu Das**[6], **Creg J. Workman**[1,3], **Dario A. A. Vignali**[1,3,11,*]

[1]Department of Immunology, University of Pittsburgh School of Medicine, Pittsburgh, PA, USA.

[2]Graduate Program of Microbiology and Immunology, University of Pittsburgh School of Medicine, Pittsburgh, PA, USA.

[3]Tumor Microenvironment Center, UPMC Hillman Cancer Center, Pittsburgh, PA, USA.

[4]Institute for Immunology, University of Pennsylvania Perelman School of Medicine, Philadelphia, PA, USA.

[5]Department of Systems Pharmacology and Translational Therapeutics, University of Pennsylvania Perelman School of Medicine, Philadelphia, PA, USA.

[6]Center for Systems Immunology, Departments of Immunology and Computational & Systems Biology, University of Pittsburgh School of Medicine, Pittsburgh, PA, USA.

[7]CMU-Pitt Joint Computational Biology, School of Medicine, University of Pittsburgh, Pittsburgh, PA, USA.

[8]Division of Rheumatology and Clinical Immunology, University of Pittsburgh School of Medicine, Pittsburgh, PA, USA.

*Corresponding Author: dvignali@pitt.edu.

&contributed equally

Author Contributions

D.A.A.V conceived, directed and obtained funding for the project; S.G, Q.Z., C.J.W. and D.A.A.V. conceptualized, designed, analyzed the experiments. S.G. and D.A.A.V wrote the manuscript with input from J.D., H.X., S.M., C.J.W., and A.R.C.; S.G. and Q.Z. performed all experiments. A.R.C. and T.T. helped conceptualize single cell RNAseq experiments and A.R.C. and S.M. analyzed the single cell RNAseq and TCRseq data. S.M. analyzed the bulk RNASeq data. J.D. and H. X. synthesized protein interaction networks and PLS-DA. E.B. aided in diabetic mouse colony maintenance, breeding, and diabetes incidence. T.T. and C.C. generated single cell libraries. C.G.L. and G.F.M. oversaw H&E staining. R.L. contributed advice for RNAseq library generation and data acquisition. E.J.W. contributed advice in experimental design and analysis; J.D. and H.X. contributed to RNAseq analysis, network analysis, and interpretation; C.J.W. contributed to experimental design, analysis, and developing mouse strains. All authors provided feedback and approved the manuscript.

Competing interests

D.A.A.V and C.J.W. declare competing financial interests and have submitted patents covering LAG3 that are licensed or pending and are entitled to a share in net income generated from licensing of these patent rights for commercial development. DAAV: cofounder and stock holder – Novasenta, Potenza, Tizona, Trishula; stock holder – Oncorus, Werewolf, Apeximmune; patents licensed and royalties – Astellas, BMS, Novasenta; scientific advisory board member – Tizona, Werewolf, F-Star, Bicara, Apeximmune, T7/Imreg Bio; consultant – Astellas, BMS, Almirall, Incyte, G1 Therapeutics, Inzen Therapeutics; research funding – BMS, Astellas and Novasenta. E.J.W. has consulting agreements with and/or is on the scientific advisory board for Merck, Roche, Pieris, Elstar, and Surface Oncology. E.J.W. has a patent licensing agreement on the PD-1 pathway with Roche/Genentech. E.J.W. is a founder of Arsenal Biosciences. The other authors declare no competing interests

[9]Department of Pathology, Brigham and Women's Hospital and Harvard Medical School, Boston, MA, USA.

[10]Parker Institute for Cancer Immunotherapy at University of Pennsylvania Perelman School of Medicine, Philadelphia, PA, USA.

[11]Cancer Immunology and Immunotherapy Program, UPMC Hillman Cancer Center, Pittsburgh PA, USA.

[12]Present address: Program in Cellular and Molecular Medicine, Boston Children's Hospital and Harvard Medical School, Boston, MA, USA.

Abstract

Impaired chronic viral and tumor clearance has been attributed to $CD8^+$ T cell exhaustion, a differentiation state in which T cells have reduced and altered effector function that can be partially reversed upon blockade of inhibitory receptors. The role of the exhaustion program and transcriptional networks that control $CD8^+$ T cell function and fate in autoimmunity is not clear. Here we show that intra-islet $CD8^+$ T cells phenotypically, transcriptionally, epigenetically and metabolically possess features of canonically exhausted T cells, yet maintain important differences. This 'restrained' phenotype can be perturbed and disease accelerated by $CD8^+$ T cell-restricted deletion of the inhibitory receptor lymphocyte activating gene 3 (LAG3). Mechanistically, LAG3-deficient $CD8^+$ T cells have enhanced effector-like functions, trafficking to the islets, and have a diminished exhausted phenotype, highlighting a physiological function for an exhaustion program in limiting autoimmunity and implicating LAG3 as a target for autoimmune therapy.

Introduction

$CD8^+$ T cell dysfunction or exhaustion is a differentiation state distinct to that of effector or memory and has been extensively studied in cancer and chronic viral infections[1]. T cell exhaustion is driven by persistent antigen exposure and chronic T cell receptor (TCR) stimulation, and is characterized by altered effector functions, reduced proliferative capacity, an altered transcriptional and epigenetic landscape, and persistent, high level expression of multiple inhibitory receptors such as programed cell death protein 1 (PD1), lymphocyte activating gene 3 (LAG3), T cell immunoglobulin and mucin domain-containing protein 3 (TIM3), and T cell immunoreceptor with Ig and ITIM domains (TIGIT)[1]. The transcription factors (TFs) Transcription Factor 1 (TCF1) and Thymocyte Selection Associated High Mobility Group Box (TOX) are critical modulators of the exhaustion program and are required to maintain progenitor populations and to transition cells to terminal exhaustion[2–6].

Autoimmunity, chronic viral infections, and cancer share two common features associated with T cell exhaustion: persistent antigen exposure and chronic TCR stimulation. However, it remains unclear whether there are differences in exhaustion programs in the context of autoimmunity versus chronic infection (lymphocytic choriomeningitis virus clone 13, LCMV Cl. 13) and cancer. There is currently much interest in defining the state of autoreactive T cells due to the therapeutic potential of targeting inhibitory receptors on

such cells. In the MRL-*lpr* mouse model of systemic lupus erythematosus (SLE), kidney infiltrating T cells have been shown to be functionally, metabolically, and transcriptionally exhausted, yet this does not prevent autoimmunity[7,8]. In human autoimmunity, high inhibitory receptor expression on T cells correlates with reduced autoimmune symptoms and, in the case of Type 1 Diabetes (T1D), responsiveness to anti-CD3 immunotherapy[9–12]. Similarly, autoimmune-related adverse events following inhibitory receptor blockade therapy in cancer patients supports the importance of inhibitory receptor function in maintaining immune homeostasis[13,14]. However, these observations remain controversial[15] and it is unclear if they are solely linked to increased inhibitory receptor expression or if an underlying transcriptional and mechanistic program related to T cell exhaustion is present, thereby inferring a physiological role for the exhaustion program in limiting autoimmunity.

T1D is a chronic autoimmune disorder characterized by immune infiltration and subsequent destruction of insulin producing β cells and is spontaneously modeled in the non-obese diabetic (NOD) mouse, providing an ideal system to study autoreactive $CD8^+$ T cells[16]. Although $CD4^+$ effector T cells are largely considered the primary drivers of T1D, there is an increasing appreciation for the role of $CD8^+$ T cells in disease progression and for a stem-like population in the pancreatic lymph nodes (pLN) that appears to renew the effector pool[15,17,18]. However, intra-islet $CD8^+$ T cells (the population that is actively destroying pancreatic β cells) exist in unique functional state to which the islet microenvironment clearly contributes[19–22]. Whereas inhibitory receptors, such as LAG3 and PD1, restrain the autoimmune response, a specific role for an exhaustion program impacting $CD8^+$ T cell pathogenicity has yet to be fully established; indeed, the existence of an ‘exhausted-like’ phenotype is still debated by some and even refuted by others[10,15,23].

Here we find a subset of ‘restrained’ intra-islet $CD8^+$ T cells that have features reminiscent of the canonically exhausted phenotype of LCMV Cl.13 and tumors, yet this population maintains some important differences. When this phenotype is perturbed through the deletion of LAG3, autoimmune diabetes incidence is accelerated, highlighting a physiological role for $CD8^+$ T cell restraint in delaying disease onset and implicating LAG3 as a potential immunotherapeutic target for the treatment or prevention of autoimmune diabetes.

Results

Autoreactive $CD8^+$ T cells express hallmarks of exhaustion

To investigate our hypothesis that the diabetic islet microenvironment may induce or promote T cell exhaustion due to chronic high antigen exposure and altered nutrient availability, we first preformed high dimensional flow cytometric analysis using Cytobank[24] (11 markers) of islet-infiltrating $CD8^+$ T cells from 12-week-old female wild type (WT) NOD mice. This analysis revealed a clear distinction between intra-islet $CD8^+$ T cells and remarkable heterogeneity within the islets, compared to the non-draining lymph node (ndLN) and pancreatic lymph node (pLN, Fig. 1a). All exhausted T cells and progenitors express TOX, while only the early progenitor sub-populations express TCF1 and terminally exhausted $CD8^+$ T cells lose TCF1 expression and further upregulate TOX[2]. High dimensional FlowSOM clustering analysis allowed us to identify clusters #1 and #3 within

the islets that expressed high levels of TOX but lacked TCF1, emblematic of a terminally exhausted phenotype (Fig. 1a, Extended data Fig. 1a–b). Interestingly, LAG3 was the only inhibitory receptor that was unique and highly co-expressed with these clusters. This analysis also revealed a similar cluster (#2) that maintained TCF1 expression, suggesting it may be an earlier progenitor population (Fig. 1a). An autoimmune progenitor population has recently been described in the pLN of NOD mice[15]. Here we show a similar population within the islets, with the addition of high inhibitory receptor expression. It is worth noting that cluster #2 lacked LAG3 expression, suggesting LAG3 is unique to more terminally differentiated sub-populations.

Given the preponderance of LAG3 expression on 'exhausted' T cells, we used this feature to interrogate the transcriptome of intra-islet $CD8^+$ T cells from *Lag3*$^{L/L\text{-}YFP}$.NOD mice (in which *Lag3* expression is marked by concordant YFP expression[25]) to determine if $LAG3^+$ intra-islet $CD8^+$ T cells are enriched for signatures of exhaustion (Extended Data Fig. 2a–b). To address this, bulk RNA sequencing (RNAseq) was performed on YFP^+ vs YFP^- intra-islet $CD8^+$ T cells (Extended Data Fig. 2a–b). Interestingly, YFP^+ intra-islet $CD8^+$ T cells express high levels of co-signaling receptors (Extended Data Fig. 2c) and are enriched for markers of exhaustion rather than markers of activation (Fig. 1b, Extended Data Fig. 2d). Studies have shown that exhausted T cells from LCMV Cl. 13 exhibit a unique epigenome[26]. Using ATACseq, we found that in comparison to ndLNs, total intra-islet $CD8^+$ T cells are enriched for an exhausted epigenome, but also appear to possess features of an effector epigenome (Fig. 1c, Extended Data Fig. 2e). Taken together, these data along with other studies[22], suggest that a subset of intra-islet $CD8^+$ $LAG3^+$ T cells exhibit features of canonically exhausted $CD8^+$ T cells.

We then used spectral flow cytometry to further assess intra-islet $CD8^+$ T cell subsets over time to correlate with disease progression. Intra-islet $CD8^+$ T cells are very heterogeneous[22]: a subset of total intra-islet $CD8^+$ T cells upregulate inhibitory receptors and TFs related to exhaustion, which increase over time, while other subsets upregulate effector and memory markers (specifically, $PD1^-$ $CD8^+$ T cells), compared to ndLN and pLN controls (Extended Data Fig. 1, 3). Interestingly, the inhibitory receptors TIM3 and CTLA4 are minimally expressed on intra-islet $CD8^+$ T cells at all timepoints, highlighting a key difference between intra-islet and canonically exhausted $CD8^+$ T cells (Extended Data Fig. 1b–d). Analysis of intra-islet $CD8^+$ T cells reveals that the majority are $TCF1^+TOX^-$ (Extended Data Fig. 1e). Indeed, when we subset by PD1 expression, we find that almost all $PD1^-CD8^+$ T cells are $TCF1^+TOX^-$, lack co-inhibitory receptor expression, and are $CD127^+KLRG1^-$ (Extended Data Fig. 3b, 4a–d), which suggests this subset is Memory Precursor Effector Cells (MPECs) and likely propagates disease. This population has been extensively documented in the literature, while exhausted cells have not in autoimmune diabetes[22,27,28]. The percent TOX^+ total intra-islet $CD8^+$ T cells correlates with the inhibitory receptors PD1, TIGIT and LAG3 (Extended Data Fig. 1f), and the percent $TCF1^-TOX^+$ $CD8^+$ T cells increases with disease progression (Extended Data Fig. 1e), indicating that a sub-population of intra-islet $CD8^+$ T cells, which increases over time, may be differentiating toward exhaustion rather than a memory or effector lineages (Extended Data Fig. 3a–e). Previous studies suggest that antigen specificity is a pre-requisite for islet trafficking and bystander T cells cannot accumulate within the islets[29]. Using Insulin and glucose-6-phosphatase catalytic

subunit-related tetramers (InsB and Nrpv7, respectively) to investigate known β cell antigen autoreactive $CD8^+$ cells, we find a similarly heterogeneous population of $tetramer^+$ $CD8^+$ T cells (Extended Data Fig. 3f–g).

Exhausted subsets of $CD8^+$ T cells are derived from a $PD1^+$ population[2]. We therefore compared intra-islet $CD8^+$ T cells based on PD1 expression (ndLN and pLN are not included in this analysis as there are few $PD1^+$ cells in the LNs, Extended Data Fig. 1) and found that a high percentage of $PD1^+CD8^+$ T cells co-express LAG3 and TIGIT, a population that increases over time (Fig. 1d–e, Extended Data Fig. 4a–b). Further analysis of TCF1 and TOX based on PD1 expression demonstrated that the majority of $PD1^+$ intra-islet $CD8^+$ T cells are either $TCF1^+TOX^+$ or $TCF1^-TOX^+$ (Fig. 1f, gating based on total or $PD1^-$ $CD8^+$ T cells, Extended Data Fig. 1e, 4c–d), implying that intra-islet $PD1^+$ $CD8^+$ T cells may possess features of exhausted progenitor states, moving toward a terminally exhausted population. The percentage of $TCF1^-TOX^+$ cells increases with time, while $TCF1^+TOX^-$ cells decreases (Fig. 1f), suggesting that with disease progression, terminally exhausted ($PD1^+TCF1^-TOX^+$) intra-islet $CD8^+$ T cells accumulate in the islets. Interestingly, the $TCF1^+TOX^+$ sub-population that was largely maintained over time (Extended Data Fig.1e, 4c–d). Taken together, our data suggest that intra-islet $CD8^+$ T cells exhibit multiple features of exhaustion.

We next profiled known $CD8^+$ T cell markers that distinguish effector (Tbet, CD73) and exhausted (EOMES, CD39) cells in LCMV Cl. 13 and tumors[30–34]. We find that very few intra-islet $CD8^+$ T cells from 12-week-old NOD mice upregulate effector marker Tbet, and only a subset (~40%) upregulate CD73 (Extended Data Fig. 4e–f). In contrast, the exhaustion markers CD39 and EOMES are enriched in intra-islet $CD8^+$ T cells compared to the LNs (Extended Data Fig. 4e–f), where islets also contain a $CD39^+EOMES^+$ sub-population (Fig. 2a). Intra-islet $CD8^+$ T cells, like those from tumors and LCMV Cl. 13, do not have a significant proportion of cells expressing CD39 and CD73 (Extended Data Fig. 4e). Interestingly, we find very few $Tbet^+$ $CD8^+$ T cells, either single positive or co-expressing EOMES (Extended Data Fig. 4f).

We next sought to understand how intra-islet $CD8^+$ T cells might be functionally impacted. Nutrient availability, metabolism, and the ability to take up glucose are important determinants of $CD8^+$ T cell function in tumors and LCMV Cl. 13[35–37]. Furthermore, mitochondrial stress (reactive oxygen species, ROS) has recently been implicated as a driver of exhaustion, while impaired glucose uptake and lower mitochondrial mass are characteristic of tumor-derived exhausted $CD8^+$ T cells[36,37]. Similarly, we observed a striking impairment in the uptake of fluorescently-labeled glucose (Glucose-Cy5) and mitochondrial mass (MitoTracker) coupled with a decrease in mitochondrial potential (Tetramethylrhodamine, TMRM) (Fig. 2b, Extended Data Fig. 4g) in intra-islet $CD8^+$ T cells compared to LN controls[36]. Interestingly, in contrast to tumor infiltrating $CD8^+$ T cells, intra-islet $CD8^+$ T cells do not show an accumulation of ROS (MitoSOX and CellROX, Extended Data Fig. 4h). Despite these severe metabolic deficiencies, intra-islet $CD8^+$ T cells maintain production of some cytokines at a level similar to LN controls and intra-islet $CD4^+$ T cells (Extended Data Fig. 4i).

Finally, we investigated possible drivers of the impaired metabolic phenotype. Given that hypoxia drives metabolic dysfunction in tumors[36], we used hypoxyprobe to assess hypoxic intra-islet CD8$^+$ T cells by flow cytometry (Methods). Interestingly, we found an accumulation of both hypoxyprobe and Hif1α in intra-islet CD8$^+$ T cells (Fig. 2c–d), with percent Hif1α correlating with hypoxyprobe (Fig. 2e). While islets are highly vascularized, hypoxia in islets has been reported and is often cited as a barrier to islet transplantation[38–41]. β cells are thought to induce localized hypoxia due to high oxygen consumption demands to produce insulin[38]. Our data suggests that hypoxia may contribute, in conjunction with other unknown nutrient deficiencies or pro-inflammatory signals, to immune dysfunction in the islets. Together, we observed phenotypic, functional, metabolic, transcriptional, and epigenetic alterations in a subset of intra-islet CD8$^+$ T cells that maintain certain features of canonical exhaustion (Fig. 2f). These data suggest that the exhaustion-like phenotype "restrains" the function of intra-islet CD8$^+$ T cells.

LAG3 limits autoimmune diabetes and promotes terminal differentiation

Given that LAG3/YFP$^+$ intra-islet CD8$^+$ T cells are transcriptionally enriched for genes related to exhaustion (Fig. 1b, Extended Data Fig. 2c–d) and that "restrained" CD8$^+$ T cell clusters #1 and #3, specifically express LAG3 (Fig. 1a), we aimed to perturb the development of this phenotype by deleting LAG3 cell surface expression specifically on CD8$^+$ T cells (*Lag3*$^{L/L\text{-}YFP}$E8i$^{CRE/CRE\text{-}GFP}$.NOD, a model in which the transmembrane domain of LAG3 is deleted in CD8$^+$ T cells, thereby allowing the secretion of soluble LAG3, which does not have a known function at this time, but preventing LAG3 expression on the cell surface and LAG3 cell intrinsic signaling, herein referred to as *Lag3*$^{\Delta TM}$ mice; Extended Data Fig. 5a–b)[25]. We hypothesized that deleting LAG3, a secondary inhibitory receptor compared to PD1, would allow us to subtly perturb the development of the restrained phenotype observed in WT intra-islet CD8$^+$ T cells. Strikingly, accelerated diabetes incidence was observed in both female and male *Lag3*$^{\Delta TM}$ mice compared to *Lag3*$^{L/L\text{-}YFP}$.NOD and E8i$^{CRE/CRE\text{-}GFP}$.NOD (herein referred to as Cre Control) mice, with all females diabetic by ~16 weeks of age (Fig. 3a).

To further resolve heterogeneous intra-islet CD8$^+$ T cell populations and to investigate the transcriptional consequences of LAG3 deletion, CD8$^+$ T cells from the islets and ndLN were isolated and subjected to 5' single cell RNA sequencing (scRNAseq), allowing us to recover paired single-cell gene expression signatures and T cell receptor (TCR) sequences. Analysis revealed 8 transcriptionally unique clusters (Supplementary Table 1), 2 of which consisting predominantly of ndLN derived CD8$^+$ T cells (clusters 1 and 5), while the remaining 6 were primarily representative of intra-islet CD8$^+$ T cells (Fig. 3b, Extended Data Fig. 5c–d). LAG3 is activation induced, so therefore genotype did not influence the clustering pattern of cells from the ndLN, but greatly influenced the clustering of intra-islet CD8$^+$ T cells with clusters 3 and 4 exhibiting enrichment for *Lag3*$^{\Delta TM}$, while clusters 6 showed enrichment for the Cre Control (Fig. 3b [colored red and blue, respectively], Extended Data Fig. 5d).

Using over-representation analyses (ORA)[42,43], we explored whether the identified gene signatures marking the intra-islet Cre Control and *Lag3*$^{\Delta TM}$ CD8$^+$ T cells were enriched for certain pathways. We used the top 50 differentially expressed genes (DEGs) characterizing

each genotype (Supplementary Table 2 and Methods) to examine enrichment in the Kyoto Encyclopedia of Genes and Genomes (KEGG)[44–46] pathway database (Extended Data Fig. 5e). We find that intra-islet *Lag3*$^{\Delta TM}$ CD8^{+} T cells show enrichment for viral infection KEGG pathways which feature effector genes such as *Fos*, *Jun*, *Jund*, *Myc* and *Nfkbia* (Extended Data Fig. 5e–f), suggesting enhanced effector function. Conversely, the intra-islet Cre Control enriched CD8^{+} T cell cluster (cluster 6) revealed KEGG pathways featuring inhibitory or apoptotic genes (e.g *Klrc1/2* [gene encoding NKG2A/C], *Klrd1* [gene encoding CD94, co-receptor for NKG2A/C], *Sh2d1a*, *Casp3*, *Ctsb*, *Ctsd*, *Bcl2a1d*; Extended Data Fig. 5e–f)[47,48]. Interestingly, both intra-islet Cre Control and *Lag3*$^{\Delta TM}$ maintained cytokine transcripts. Importantly, analysis of intra-islet CD8^{+} T cells revealed a distinct transcript in the absence of LAG3. Finally, we assessed these distinct phenotypes in the context of previously established CD8^{+} T cell dysfunction in tumors[26]. Using gene set enrichment analysis (GSEA), we find that *Lag3*$^{\Delta TM}$ dominated clusters, 3 and 4, are transcriptionally more progenitor-like, while Cre Control dominated cluster 6, is enriched for a terminal exhaustion score (Fig. 3c).

To further assess these differences, we used pseudotemporal modeling (Methods)[49,50] to infer differentiation trajectories across genotypes. Pseudotime analysis revealed one continuous trajectory of differentiation (Fig. 3d). This differentiation trajectory begins with genes associated with naivety including *Sell* (gene encoding CD62L), *Ccr7, Klf2,* and *Lef1* (Fig. 3d–e, Extended Data Fig. 6a–b), and progresses towards genes associated with exhaustion and those characteristic of Cre Control intra-islets cells, including *Klrc1/2, Bcl2a1d, Pdcd1, Tigit,* and *Lag3* (Fig. 3e, Extended Data Fig. 6c–d). These data indicate that the diffusion pseudotime trajectory begins at low values of diffusion component 1 (DC1), occupied by naïve cells, and progresses through the linear trajectory to terminal differentiation which is correlated with upregulation of exhaustion-related signatures and downregulation of naïve related signatures, consistent with the intra-islet exhausted-like phenotype identified by our flow cytometry experiments. As anticipated, genes associated with the middle of pseudotime appear to be related to CD8^{+} T cell effector function and are associated with the *Lag3*$^{\Delta TM}$ ORA: *Fos, Jun, Junb, Jund, Nfkbia, Irf7* (Fig. 3e, Extended Data Fig 6c). It is worth noting that TOX was a top DEG in islet clusters 2 (~50/50 split per genotype) and 6 (Cre Control enriched) but was not in clusters 3 and 4 (*Lag3*$^{\Delta TM}$ dominated clusters, Supplementary Table 2). TOX was also expressed through middle and late pseudotime, likely due to its upregulation in exhausted progenitor populations as well as terminal populations (Extended Data Fig 6c–d). As predicted by the genes dictating pseudotime (Fig. 3e, Extended Data Fig 6b–d), intra-islet Cre Control CD8^{+} T cells occupy the space in late pseudotime, while *Lag3*$^{\Delta TM}$ CD8^{+} T cells more frequently occupy an earlier position in the inferred differentiation trajectory (Fig. 3f, Extended Data Fig. 6a). Together, these data confirm that LAG3 expression limits effector potential and promotes a more terminally differentiated phenotype (Fig. 3f).

We next interrogated the relationship between TCR clonality, gene expression, and differentiation states of CD8^{+} T cells. Initially, we found trends toward increased activation (indicated by clonal expansion) amongst intra-islet *Lag3*$^{\Delta TM}$ CD8^{+} T cells (Extended Data Fig. 7a) as well as expanded TCR repertoire, suggestive of a broader CD8^{+} T cell response (Extended Data Fig. 7b, Supplementary Table 3). We sought to characterize the

differentiation states of clonally expanded TCRs within the islets between the *Lag3*$^{\Delta TM}$ and Cre Controls. We visualized the clonally expanded TCRs (i.e. TCRs with greater than 4 clones) along the DC1 axis, and found that enhanced clonality was coupled to a less terminally differentiated transcriptional state in the *Lag3*$^{\Delta TM}$ CD8^{+} T cells (Fig. 3g). In summary, single-cell TCR analysis revealed (1) trends toward a higher frequency of clonally expanded TCRs, (2) trends toward a higher number of unique clones, and (3) a more progenitor differentiation status in those clonally expanded *Lag3*$^{\Delta TM}$ intra-islet CD8^{+} T cells.

To explore the functional consequence of positioning in pseudotime differentiation between *Lag3*$^{\Delta TM}$ and Cre Control, we divided the diffusion pseudotime trajectory into 5 clusters according to the embedding in DC 1 and 2, aiming to determine genes that characterize the differentiation trajectory in each genotype (Extended Data Fig. 7c). When specifically looking at clusters enriched in the islets (i.e. clusters 3 through 5), we found that markers of restrained CD8^{+} T cells (*Batf* and *Klrc1*) are associated with terminal differentiation and are more highly expressed in Cre Control mice, while chemokine receptors *Cxcr6/3* are associated with intermediate pseudotime and more highly expressed in *Lag3*$^{\Delta TM}$ (Extended Data Fig. 7d). These findings are consistent with more effector-like CD8^{+} T cells driving accelerated diabetes in *Lag3*$^{\Delta TM}$ mice.

Lag3$^{\Delta TM}$ cells have a less restricted interactome than Cre controls

We further contextualized the genotype-specific expression signatures (Extended Data Fig. 5e–f) using protein-protein interactions (PPIs) involving proteins encoded by these genes. Protein interactomes provide an orthogonal and unbiased way to assess functional differences between the Cre Control and *Lag3*$^{\Delta TM}$ intra-islet CD8^{+} T cells. We used HINT – a widely-used database of PPIs in human and model organisms[51] to identify the relevant interactions. HINT uses previously established criteria[52] to combine literature-curated and high-throughput interaction datasets with each edge in the corresponding protein interaction network based on multiple lines of experimental evidence[51]. Using the binary and co-complex murine protein interactome networks from HINT in conjunction with the genotype-specific expression signatures, we identified subnetworks characterizing the Cre Control and *Lag3*$^{\Delta TM}$ CD8^{+} T cells (Extended Data Fig. 8, Supplementary Table 4).

We observed notable differences in the overall structure of these subnetworks. Genes with higher expression levels in *Lag3*$^{\Delta TM}$ CD8^{+} T cells (i.e., seed genes for the *Lag3*$^{\Delta TM}$ subnetwork) encoded proteins with a higher number of interactors on average (i.e., higher average connectivity) than genes with higher expression levels in the Cre Control cells (i.e., seed genes for the Cre Control subnetwork, Extended Data Fig. 8, Supplementary Table 4). This suggests that genes encoding proteins characterized by *Lag3*$^{\Delta TM}$ cells have the ability to interact with an expanded repertoire of proteins than those characterizing the Cre Control intra-islet CD8^{+} T cells, and therefore, may be involved in a wider array of functions, consistent with a more effector-like transcriptional program. Further, we explored the overall connectivity structure (i.e., the degree distribution of number of interaction partners for the proteins encoded by the genes) and found that proteins encoded by genes in the *Lag3*$^{\Delta TM}$ signature tended to have higher degree than those in the Cre Control signature

(Extended Data Fig. 8c). Taken together, our bioinformatic analyses, including ORA, GSEA, diffusion pseudotime, and network analyses, suggest that LAG3 expression promotes a more terminally differentiated state and serves to restrict effector function by promoting a more inhibited and limited transcriptome.

LAG3 limits function and accumulation of intra-islet CD8$^+$ T cells

We sought to confirm our bioinformatic observations at the protein, cellular and mechanistic level. Consistent with diabetes incidence (Fig. 3a), *Lag3*$^{\Delta TM}$ mice have increased islet infiltration by insulitis scoring (Fig. 4a). This is reflective of an increase in CD8$^+$ T cells, by both percent and cell number (Fig. 4b). Of note, *Lag3*$^{\Delta TM}$ CD8$^+$ T cells had a slight survival advantage by decreased cleaved caspase 3, and a modest proliferative advantage by Ki67$^+$BrdU$^+$, though BCL-2 remained unchanged (Extended Data Fig. 9a–b). Coupled to an increased cell number, we observed an increased expression of CXCR3 and CXCR6 protein expression in the *Lag3*$^{\Delta TM}$ CD8$^+$ T cells, suggesting that enhanced trafficking or retention in the islets might function as a mechanism for accumulation in the islets (Fig. 4c).

Given the complexity and temporal heterogeneity of diabetes onset in NOD mice, we sought to determine if a multivariate partial least squares discriminant analyses (PLS-DA) model that incorporates markers of both exhaustion and activation can accurately stratify NOD mice by genotype. Using the markers CD44, CTLA4, TOX, PD1, TCF1, and TIGIT (assessed by flow cytometry), PLS-DA analysis reveals a significant discrimination between intra-islet Cre Control (expressing higher TOX, PD1, and TCF1) and *Lag3*$^{\Delta TM}$ (expressing higher CD44, CTLA4 and TIGIT, Fig. 4d, Extended Data Fig. 9c). Traditional flow gating confirms *Lag3*$^{\Delta TM}$ CD8$^+$ T cells express significantly higher markers of activation (CD44 and KLRG1) and have an increase in polyfunctionality by (IFNγ^+TNFα^+) (Extended data Fig. 9d, 10b). Conversely, markers of terminally exhausted sub-populations, such as PD1 and TOX, or EOMES and CD39 co-expression were decreased in tetramer$^+$ CD8$^+$ T cells and the pLN respectively (with trends observed in bulk intra-islet CD8$^+$ population, Extended Data 9e).

Finally, the metabolic function and single cytokine production of intra-islet CD8$^+$ T cells seemed only modestly affected by LAG3 deletion (Extended Data Fig. 10a–c). Although some aspects of exhaustion are not modulated by LAG3 deletion, it appears that LAG3 limits diabetogenic potential by promoting a restrained phenotype.

LAG3 restricts recognition of secondary antigens

We last sought to assess any differences in antigen recognition between *Lag3*$^{\Delta TM}$ and Cre Control CD8$^+$ T cells as a metric for disease progression. Insulin is thought to be a primary target of effector T cells in autoimmune diabetes, followed by recognition of secondary epitopes, such as IGRP, through epitope spreading[53,54]. A similar percentage of intra-islet CD8$^+$ T cells from Cre Control and *Lag3*$^{\Delta TM}$ mice were specific for insulin, as determined by InsB$^+$ tetramer staining (~5%), however, we found that *Lag3*$^{\Delta TM}$ CD8$^+$ T cells have dramatically increased antigen specificity for IGRP (Nrpv7$^+$ tetramer staining, ~10% Fig. 4e, Extended Data Fig. 10d), implying that LAG3 may limit epitope spreading and thus disease progression[55–57]. Furthermore, IGRP-reactive *Lag3*$^{\Delta TM}$ CD8$^+$ T cells are enriched

for and correlate to the percentage of short-lived effector cells ($KLRG1^+CD127^-$, Fig. 4f), consistent with a more pathogenic, less restrained phenotype. Analysis of $tetramer^+$ cells suggest that LAG3 may restrain disease progression by limiting epitope spreading.

Collectively, our data suggest that LAG3 expression limits: (1) $CD8^+$ T cell trafficking into the islets, (2) effector phenotype, (3) survival and proliferation, (4) polyfunctionality and (5) may limit epitope spreading (Fig. 4g). Collectively, our data support a model in which LAG3 limits disease by enhancing the 'restrained' $CD8^+$ T cell phenotype and promoting terminal differentiation.

Discussion

Our study highlights five important observations that affect our current understanding of $CD8^+$ T cell function and pathogenesis in autoimmune diabetes. (1) We reveal the presence of intra-islet exhausted-like $CD8^+$ T cell, termed restrained $CD8^+$ T cells, which is similar, yet maintains key differences to canonical T cell exhaustion. We expand on the current understanding of T cell exhaustion in autoimmunity to show that at least a subset of intra-islet $CD8^+$ T cells are phenotypically, epigenetically, transcriptionally, and functionally restrained by an exhaustion-like program. However, we also show that autoreactive, restrained $CD8^+$ T cells retain some functionality, which given the chronicity of autoimmune diabetes, may still allow for destruction of non-replicative β cells over time.

(2) We show that $CD8^+$ T cell restraint is vital to delaying disease onset, as exemplified by the consequence of highly accelerated diabetes onset when that restrained phenotype is perturbed through LAG3 deletion. Indeed, $Lag3^{\Delta TM}$ are more effector-like in function, suggesting LAG3 expression is required for terminal restraint and to limiting an accumulation of a highly diabetogenic population of $CD8^+$ T cells. Recently, a stem-like $CD8^+$ T cell population was reported in the pLNs[15]. We clearly show this $TCF1^+$ population also exists in islets and likely hosts an effector pool, but we add to this study by highlighting a $TCF1^+TOX^+$ and $TCF1^-TOX^+$ populations that resemble canonical exhaustion progenitors. Induction of this restrained population may be harnessed as a therapeutic approach to treating autoimmune diabetes. While our studies are limited to the NOD model, further studies could investigate $CD8^+$ T cell restraint and the consequences thereof in other autoimmune settings.

(3) LAG3 deletion in $CD8^+$ T cells leads to enhanced recognition of secondary islet antigens, clonal expansion, and number of unique TCR clones. This suggests LAG3 expression may limit epitope spreading, avidity maturation, and disease progression in islet reactive $CD8^+$ T cells, though additional studies would be required to further support this notion[55–57].

(4) LAG3 single deletion or blockade alone has a minimal effect on immune response to tumors or LCMV Cl. 13, where it only has a significant and synergistic role when combined PD1 blockade or deletion[58–60]. In striking contrast, LAG3 single deletion from the surface of $CD8^+$ T cells is sufficient to accelerate autoimmune diabetes substantively, reminiscent albeit slightly delayed to that observed in LAG3 global knockout NOD, or

WT NOD treated with anti-LAG3[23]. Interestingly, LAG3 single deletion from the surface of regulatory T (Treg) cells has the opposite effect: these mice are protected against autoimmune diabetes[25]. Therefore, the interpretation of the LAG3 global KO or WT NOD treated with anti-LAG3 accelerated diabetes phenotype must be driven by $CD8^+$ T cells and effector $CD4^+$ T cell activation which can out compete any beneficial effects LAG3 deletion on Treg cells. LAG3 deletion clearly alters the developmental state of intra-islet $CD8^+$ T cells, where it does not in tumors or LCMV, suggesting that LAG3 plays a more impactful role in limiting autoimmunity and implicating agonistic signaling through LAG3 as an avenue for future autoimmune therapeutics[61]. Indeed, recent reports in human autoimmunity (Multiple Sclerosis and T1D) support our findings regarding the reliance on LAG3 to limit autoimmunity[62].

(5) Our study supports the previously reported notion that although autoimmune diabetes is traditionally thought of as a $CD4^+$ T cell mediated, $CD8^+$ T cells can contribute substantively to disease progression, opening an underappreciated opportunity for $CD8^+$ T cell targeted immunotherapy to ameliorate disease. Indeed, modest phenotypic changes can result in dramatic differences in disease onset in our *Lag3*$^{\Delta TM}$ NOD model, suggesting that modest therapeutically induced changes in autoreactive $CD8^+$ T cells may dramatically influence disease outcomes.

An interesting distinction between $CD8^+$ T cells in tumors and LCMV versus autoimmunity is that they inhibit disease clearance in the former but allow for disease progression in the latter, highlighting the difference between the exhaustion and restrained phenotypes detailed herein. Restrained $CD8^+$ T cells in the islets produce cytokine and appear to retain proliferative potential. The extent to which they contribute to β cell destruction is yet unclear and should be a focus of future studies. Together, our data suggest that autoreactive T cells can exhibit a ‘restrained’ phenotype that delays, but cannot prevent overt autoimmunity. Future studies should focus on specific mechanisms of inducing restraint. Our observations suggest that inhibitory receptor agonism could have a bigger therapeutic index for the treatment of autoimmunity than previously appreciated.

Methods

Mice and study design

NOD/ShiLtJ (stock #001976), NOD mice were purchased from the Jackson Laboratory. E8i$^{CRE/CRE-GFP}$ C57BL/6 mice were provided by the Littman (The Kimmel Center for Biology and Medicine of the Skirball Institute, New York University School of Medicine, New York, NY USA, Howard Hughes Medical Institute, New York, NY, USA) and Taniuchi (Laboratory for Transcriptional Regulation, RIKEN Center for Integrative Medical Sciences (IMS), 1–7-22 Suehiro-cho, Tsurumi-ku, Yokohama, 230–0045, Japan) labs and were bred onto a NOD background at St. Jude Children’s Research Hospital. Microsatellite analysis revealed 99.6% NOD, having one heterozygous SNP on chromosome 16. *Lag3*$^{L/L-YFP}$.NOD were generated and bred onto the NOD background[25]. *Lag3*$^{L/L-YFP}$.NOD and E8i$^{CRE/CRE-GFP}$.NOD were then crossed to be homozygous (*Lag3*$^{L/L-YFP}$E8i$^{CRE/CRE-GFP}$.NOD, annotated in the text as *Lag3*$^{\Delta TM}$ for simplicity), expressing 2 copies of the E8i^{CRE} to obtain optimal deletion efficiency.

Controls similarly maintain 2 copies of E8i^{CRE} (E8i$^{CRE/CRE-GFP}$.NOD, are annotated E8i$^{CRE-GFP}$.NOD or “Cre Controls” in the text for simplicity)

All animal experiments were performed in the Association for Assessment and Accreditation of Laboratory Animal Care International (AAALAC)–accredited, specific pathogen–free facilities in the Division of Laboratory Animal Resources of the University of Pittsburgh School of Medicine (UPSOM). Animal protocols were approved by the Institutional Animal Care and Use Committees (IACUC) of UPSOM. Mice were housed in SPF conditions with filtered air, watering system, and 12hr light/dark cycle. The temperature and humidity dictated by DLAR/IACUC, cages are changed once per week. NOD mice in the UPSOM facility are kept isolated from any C57BL/6 in the facility, and are fed special diet to maintain a similar diabetes incidence rate to what was maintained at St. Jude Children’s Research Hospital: http://www.labsupplytx.com/wp-content/uploads/2012/10/5013.pdf (Lab Supply TX, Cat #5013). Mice have continuous access to this diet. Mice of different groups were co-housed and randomly assigned to analyses.

Ten to 30 mice per group were used in diabetes incidence studies and followed up to 30 weeks of age. Three to six age-matched (within 7 days) mice per group were used in each analytical experiment, and one to four independent experiments were repeated. Only female mice are used in analysis because of the predictable development of autoimmune diabetes[66]. Three 8-week-old female mice per group were pooled and used in bulk RNA-seq analyses, and two independent experiments were repeated. Four 8-week-old female mice per group were pooled and used in paired 5’ single cell RNAseq and TCRseq analyses. The genotypes were not blinded, except for the insulitis scoring. All data points were presented unless otherwise noted in figure.

Measurement of diabetes and insulitis

Diabetes incidence and Insulitis were monitored on co-housed animals weekly by urine and blood glucose levels. A positive urine strip test using Diastix (Bayer) necessitated blood glucose level testing by Breeze2 glucometer (Bayer). A blood glucose level of ≥400 mg/dL was considered diabetic and sacrificed.

Pancreata taken for insulitis were fixed in formalin overnight prior to storage in 70% isopropanol. Pancreata were embedded in a paraffin block and cut into 4-μm thick sections at 150-μm step sections and stained with hematoxylin and eosin. Samples were collected at UPSOM and embedded/stained at Harvard University, Department of Pathology, Brigham and Women’s Hospital. Insulitis was scored in house at UPSOM. An average of 60 to 100 islets per mouse were scored in a blinded manner. Two methods of insulitis measurement were used as described[66].

Islet isolation and lymphocyte preparation

Islets were isolated and lymphocytes excised in accordance with previous publications[25,66]. 3 mL of Collagenase Type IV solution - 600U/mL in complete Hanks’ balanced salt solution (cHBSS, Corning) with 10% fetal bovine serum (FBS) - are injected into clamped pancreatic duct. Perfused pancreata were then excised and incubated in 4 mL of the collagenase solution at 37°C for 30 minutes. Each pancreas is then washed with HBSS with 10%

FBS and spun down at 1000rpm for 3 minutes, twice, thereby mechanically breaking up the pancreas. Pancreas samples were then resuspended in clear cHBSS with 10% FBS. Islets were picked by hand under a dissecting microscope and dissociated with 1 mL cell dissociation buffer (Life technologies). Islet isolation by hand ensures a pure, β cell reactive, population of lymphocytes is collected, with minimal exocrine pancreas tissue contaminating the sample. Alternative methods for harvesting intra-islet lymphocytes from the pancreas are “dirtier” and may confound subsequent analyses. Previous publications suggest that the exocrine tissue of a diabetic pancreas has immune infiltration[67]. Therefore, attempts at isolating intra-islet $CD8^+$ T cells in the NOD model through bulk pancreas digestion likely has contaminating lymphocyte populations, as well as other pancreatic tissue that confounds analysis and makes it more challenging to isolate lymphocytes of interest in the disease progression of autoimmune diabetes. Cells in dissociation buffer are incubated for 15 minutes at 37°C, with vortexing every 5 minutes, to create a single cell suspension. Once dissociated, cells were washed in 10 mL cHBSS+FBS and used for experiments.

Antibodies and protocol for flow cytometry

Single-cell suspensions were stained with antibodies/mitochondrial stains against: CD8β (H35–17.2, BD Biosciences, Cat# 740278, Dilution Factor, DF: 1:500), Thy1.2 (53–2.1 BioLegend, Cat# 140319, 30-H121 BioLegend, Cat#’s: 140317, 105328, 105306, DF: 1:500), PD1 (RMP1–30, BioLegend Cat# 109110, BD Biosciences Cat# 749306, DF: 1:200–250), TCF1 (C63D9, Cell Signaling Cat# 9066S, DF: 1:200), CD44 (IM7, BioLegend Cat# 103026, DF: 1:200), CD62L (MEL-14, BioLegend Cat# 104433, DF: 1:200), CTLA4 (UC10–4B9, BioLegend Cat# 106323, 106323, DF: 1:200, intracellular), CD127 (A7R34, BioLegend Cat# 135043, DF: 1:200), ICOS (C398.4A, BioLegend Cat# 313548), LAG3 (4–10-C9, made and conjugated in-house to AF647 or PeCy7, DF depends on concentration of purified antibody), CD4 (GK1.1, BD Biosciences Cat# 564667, Biolegend Cat# 100451, 100408, DF: 1:500) Foxp3 (FJK-16s, eBioscience Cat# 11–5773-82, DF Fortessa: 1:200, DF Cytek: 1:100), KLRG1 (2F1/KLRG1, BioLegend Cat# 138429, 138416, DF Fortessa: 1:500, DF Cytek: 1:200), TIGIT (GIGD7, eBioscience Cat# 46–9501-82, DF: 1:200–250), TOX (REA473, Miltenyi Cat# 130–118-335, DF: 1:200), TIM3 (RMT3–23, BioLegend Cat# 1197338, DF: 1:100), aCaspase3 (D3E9 Asp175, Cell Signaling Cat# 8788S, DF: 1:200), BrdU (clone Bu20a, eBioscience Cat# 11–5071-42, DF: 1:200), BCL-2 (clone BCL/10C4, BioLegend Cat# 633510, DF: 1:200), Ki67 (B56, BD Biosciences Cat# 561284, DF: 1:200), CD107a (1D4B, Biolegend Cat# 121617, DF: 1:200), TNFα (MP6-XT22, BioLegend Cat# 506329, DF:1:200), IL-2 (JES6–5H4, Biolegend Cat# 503806, DF:1:200), IFN-γ (clone XMG1.2, Biolegend Cat# 505810, DF: 1:200), GranzymeB (NGZB, eBiosciences Cat# 46–8898-82, DF: 1:200), MitoTracker Deep Red-FM (ThermoFisher Cat# M22426, 5nM final concentration), Tetramethylrhodamine (TMRM, ThermoFisher Cat# T668, 25nM final concentration), Tetramethylrhodamine, Ethyl Ester, Perchlorate (TMRE, Cat# T669, ThermoFisher, 20nM final concentration) CellROX Deep Red (ThermoFischer Cat# C10422, 5uM final concentration), MitoSOX (ThermoFischer Cat# M36008, 5uM final concentration), GlucoseCy5 (0.4 uM final concentration, a Cy5-linked 1-amino-glucose tracer, was synthesized by the Delgoffe lab in collaboration with M. Bruchez[68], gifted to us from the Delgoffe Lab), Hypoxyprobe (clone 4.3.11.3, Hypoxyprobe Cat# HP10–1000kit), Tbet (4B10, Biolegend Cat# 644835, DF: 1:100), EOMES (Dan11mag, eBiosciences Cat#

46–4875-82, DF: 1:100), CD39 (24DMS1, Biolegend Cat# 56–0391-82, DF: 1:200), CD73 (TY/11.8, Biolegend Cat# 127222, DF: 1:200), HIF1α (IC1935P, R+D Cat# IC1935P, DF: 1:200), CXCR3 (CXCR3–173, Biolegend Cat# 126521, DF: 1:250), CXCR6 (SA051D1, Biolegend Cat# 151115, DF 1:250), HP-Biotin primary antibody (1:100, clone 4.3.11.3, from Hypoxyprobe biotin kit HP10–200kit).

Ghost viability dye was stained in the dark for 15 minutes at room temperature in PBS (Tonbo Biosciences). Surface staining (without tetramer) was performed on ice for 15–25 minutes in the dark in FACS buffer (PBS, Sodium Azide, FBS). Surface staining with tetramer was performed at room temperature in complete HBSS with 10% FBS, covered, for 45 minutes. The NRPv7 tetramer, $IGRP_{206–214}$ mimotope (KYNKANVFL/H-$2K_d$), and the InsulinB tetramers, $InsB_{15–23}$ G9L and V mimotope (LYLVCGERL/V/H-$2K^d$) were obtained from the National Institutes of Health Tetramer Core Facility. Tetramers were stained 1:250 total (1:500 for each InsB G9L and V tetramer). Cytokine expression analysis was performed ex vivo, following 5-hour stimulation with phorbol 12-myristate 13-acetate (PMA) (0.1 μg/ml; Sigma) and ionomycin (0.5 μg/ml; Sigma) in cRPMI containing 10% FBS and brefeldin A (BFA, 1:1000 dilution, Golgi Plug, BD Biosciences). For cytokine staining, BFA 1:1000 dilution is included in viability stain as well as in surface staining to ensure retention of cytokines.

For intracellular staining of cytokines and transcription factors, cells were first viability and surface stained, and washed prior to being fixed in Fix/Perm buffer (eBioscience) for 45 minutes to 2 hours. Cells were washed twice in permeabilization buffer (eBioscience) and intracellular stained for 45 minutes on ice in the dark in permeabilization buffer (eBiosciences). Following this, cells were resuspended in FACS buffer for analysis.

BrdU analysis was performed by injecting 2 mg of BrdU (Sigma) in PBS intraperitoneally 12 hours ahead of experiment. After viability, surface, Fix/perm, and intracellular staining as outlined above, cells were incubated in Cytofix/Cytoperm buffer (BD Biosciences) for 10 min at room temperature, washed with Perm/Wash buffer (BD Biosciences), treated with deoxyribonuclease I (650 U/ml; Sigma) for 30 min at 37°C, and stained with anti-BrdU antibody in Perm/Wash buffer for 30 min at room temperature.

GlucoseCy5, CellROX and MitoSOX were applied to single cell suspensions in Serum-Free HBSS at 37°C for 45 minutes, prior to viability and surface staining. Mitotracker and TMRM were included in surface stain. Cells are run immediately after surface staining as metabolic dyes are not fixable.

Hypoxyprobe analysis was performed by injecting 2 mg of Pimonidazole HCl in PBS intravenously 90 minutes prior to harvesting tissue (using Hypoxyprobe biotin kit). Pimonizazole HCL forms adducts with hypoxic tissues and can be detected by flow cytometry. Tissues are then processed as normal, lymphocytes are isolated, viability stained, surface stained, fixed and permeabilized (eBioscience), and intracellular stained overnight using HP-Biotin primary antibody (1:100, clone 4.3.11.3, in 1x permeabilization buffer). Cells were washed the next morning and stained for 45 mins on ice with streptavidin

linked APC-Cy7 secondary antibody. Cells are washed and resuspended in FACS buffer for analysis.

Cell sorting and flow cytometry analysis

Cells were sorted using Aria II (BD Biosciences) or were analyzed using Fortessa (BD Biosciences) or Cytek Aurora (Cytek Biosciences) and data analysis was performed on FlowJo versions 9 and 10 (BD Biosciences) or Cytobank Premium for subsequent Cytek data analysis. Finally, Simplified Presentation of Incredibly Complex Evaluations (SPICE)[69] plots were used to compare exhaustion marker expression from 6 to 12 weeks of age.

High dimensional analysis of our spectral flow cytometry (Cytek data) was preformed using Cytobank Premium (https://cytobank.org)[24]. FCS files for 12-week-old female WT NODs were down-sampled and concatenated in FlowJo to ensure equal number of total events from each of the 10 mice. Files were uploaded into Cytobank and traditional flow cytometry gating was performed to gate Lymphocytes, single cells, Live, $CD8^+$ T cells. viSNE analysis was performed on live, Thy1.2+ $CD8^+$ T cells using equal sampling cells from each concatenated FCS files (ndLN, pLN and Islet) to equal 100,000 total events with 1000 iterations, a perplexity of 30, and a theta of 0.5. The following markers were used to generate the viSNE maps: TOX, TIM3, CD44, PD1, CD62L, CD127, ICOS, KLRG1, LAG3, TCF1, TIGIT. The resulting viSNE maps were used to generate FlowSOM clustering. A new self-organizing map (SOM) was generated using hierarchical consensus clustering on the tSNE axes. The SOM contained 100 clusters and 10 metaclusters for $CD8^+$ T cells were identified.

PLS-DA based visualization using cell percentages

We utilized the cell percentage of the 6 cell surface markers in islet cells, gated on $CD8^+$ T cells, as features for the partial least squares discriminant analysis (PLS-DA). The cell percentages were measured by flow cytometry and quantified by subsequent FlowJo analyses. To obtain insights into the multivariate discriminative power (to distinguish between WT and LAG3 KO) of the six markers, we performed a PLS-DA using the 6 features. We assessed model performance using cross-validation, and significance using permutation testing. The relative importance of each feature was computed using the variable importance in the projection (VIP) metric. PLS was implemented in R using the plsr function; VIP scores were calculated using the vip package.

Proliferation assay

Tissues were harvested and cells were processed to single cell suspension. Cells were surface and viability stained for sorting, along with labeled with Cell Trace Violet (ThermoFischer). Cells were sorted on Lymphocytes, single cells, live, $Thy1.2^+$ $CD8^+$ T cells. Cells were sorted directly into 96-well round bottom plate containing 100uL of stimulation media (cRPMI+10%FBS, .05ug/mL αCD3/CD28, 200U/mL IL-2). 10,000 $CD8^+$ T cells were sorted from ndLN and pLN samples. The entire islet samples were sorted. For most islet samples, >5,000 $CD8^+$ T cells were obtained. Cells were cultured for 60hrs and analyzed by flow cytometry.

Single cell multiome ATAC and gene expression and analysis

$CD8^+$ T cells were isolated from the islets and ndLN of 4 $E8i^{CRE\text{-}GFP}$.NOD (8-week females). Samples were viability stained in PBS and surface stained for sorting in sort buffer (contains PBS, EDTA, BSA and HEPEs) with 10% normal mouse serum. Cells were sorted on Lymphocytes, single cell, $Thy1.2^+$, $CD8^+$ T cells. Cells were sorted into 1.5 mL Eppendorf tubes containing cRPMI and nuclei were isolated in accordance with the Nuclei Isolation for Single Cell ATAC Sequencing 10x Genomics demonstrated protocol, using the adaptations for low cell number input. Nuclei suspended in 0.04% bovine serum albumen (BSA, Sigma), counted using Cellometer Auto2000 (Nexcelom), and loaded into Single Cell Chip and processed through 10X controller for droplet generation and Library preparation.

scATACseq and RNAseq library preparation

10x genomics 5′ Gene Expression + ATAC Sequencing libraries were generated as described in the User's Guide for Chromium Next GEM Single Cell Multiome ATAC + Gene Expression Reagent Kits User Guide. In brief, nuclei were incubated in a Transposition mix that includes Transposases which enter the nuclei and fragment DNA in open regions of chromatin, while simultaneously adapter sequences are added to the fragments. Single Cell Multiome ATAC + GEX Gel Beads capture the adaptor sequences on DNA fragments as well as the poly-A tail of mRNA and GEMs are generated and incubated, resulting in 10x Barcoded DNA from the transposed DNA (for ATAC) and 10x Barcoded, full-length cDNA from poly-adenylated mRNA (for GEX). cDNA was then purified, amplified, and sequenced as per the manufacturer's recommendations (10X Genomics).

scATACseq downstream analysis

scATACseq sequenced libraries as part of the 10x Genomics ATAC+GEX assay were processed using *cellranger-arc-2.0.0.* Bigwig files for the ATAC cut sites from the output were used to visualize previously generated chromatin accessible sites in CD8 T cells d8 post LCMV armstrong infection (Effector) and d30 post LCMV Cl. 13 infection (Exhausted)[64] using *PlotHeatmap* (https://deeptools.readthedocs.io/en/develop/content/tools/plotHeatmap.html).

Gene expression profiling by bulk RNAseq and bioinformatics

YFP^+ and YFP^- $CD8^+$ T cells from the islets and YFP^- $CD8^+$ T cells from non-draining lymph node controls were sorted and pooled from three 8wk-old female *Lag3*$^{L/L\text{-}YFP}$.NOD mice. Five hundred cells per sample were used for cDNA preparation following the Smart-seq2 protocol as previously described[70]. Two independent experiments were repeated. Sequencing libraries were prepared using the Nextera XT DNA Library Prep Kit (Illumina), normalized to 2 nM using tris-HCl (10 mM; pH 8.5) with 0.1% Tween 20, diluted and denatured to a final concentration of 1.8 nM using the Illumina Denature and Dilute Libraries for the NextSeq 500 protocol Revision D (Illumina). Cluster generation and dual-indexed sequencing was performed on the Illumina NextSeq 500 system using the NextSeq 500/550 High Output v2 75 cycles Kit (Illumina).

RNA sequencing reads were aligned to GRCm38/mm10 build of Mus musculus genome using STAR-2.5.2a[71]. The Unique mapped reads were normalized using PORT (https://github.com/itmat/normalization/wiki) and counts were converted to log2 counts per million, quantile normalized and precision weighted with the 'voom' function of the limma package[72,73]. A linear model was fitted to each gene, and empirical Bayes moderated t-statistics were used to assess differences in expression[74]. P values from Bayes moderated t-tests were adjusted to control the global false discovery rate (FDR). Genes were called differentially expressed if they achieved an FDR of 0.05 or less. Heatmaps were created using R (3.5.1) package pheatmap_1.0.12 and volcano plot was created using ggplot 2_3.1.0. Gene set enrichment analysis (GSEA)[75,76] was performed against custom CD8 gene signatures[65].

CD8-specific gene signatures were created using datasets corresponding to traits of naïve, effector, memory, and exhaustion as described in the LCMV infection model (GSE41867)[65]. The Normalized enrichment score plot from GSEA for the LCMV genes signatures were plotted using GraphPad Prism.

Gene expression and TCR profiling by 5' single cell RNAseq

$CD8^+$ T cells were isolated from the islets and ndLN 4 *Lag3*$^{L/L\text{-}YFP}$E8i$^{CRE\text{-}GFP}$.NOD and 4 E8i$^{CRE\text{-}GFP}$.NOD (8-week females). Samples were viability stained in PBS and surface stained for sorting in sort buffer (contains PBS, EDTA, BSA and HEPEs) with 10% Normal mouse serum. In the surface stain of each individual sample, combinations of 1–2 CD45 cell hashing antibodies (Biolegend, TotalSeq–C0301–305) were spiked in to label each individual sample. Cells were incubated for 30 minutes on ice and washed twice prior to sorting on live, $TCRb^+$, $CD8b^+$. All $CD8^+$ T cells from islets were sorted into one 15 mL conical with cRPMI, while ndLNs were pooled in another. $CD8^+$ T cells were spun down and resuspended in 0.04% bovine serum albumen (BSA, Sigma) counted using the Cellometer Auto2000 (Nexcelom) and loaded into Single Cell Chip and processed through 10X controller for droplet generation and Library preparation.

10x genomics library preparation for 5' scRNAseq and TCRseq

10x genomics 5' Single Cell V(D)J + 5′ Gene Expression + Feature Barcode Technology libraries were generated as described in the User's Guide for 10x Chromium Single Cell V(D)J Reagent Kits with Feature Barcoding technology for Cell Surface Protein. In brief, cells were subjected to in-drop lysis and reverse transcription, generating cDNA derived from mRNA in each cell and from the oligo tagged cell hashing antibody, bearing bead-specific sequences to identify the cell of origin. cDNA was then amplified, and SPRI selection was performed for downstream library construction for gene expression, TCR sequencing, and feature barcode generation. For cDNA amplification, 2 uL of amplified cDNA product was used to selectively amplify TCR regions. Gene expression and amplified TCR libraries were then subjected to enzymatic fragmentation, end repair, A-tailing, ligation to adaptors, and sample indices by PCR. Samples are cleaned up by SPRI selection and quantified by BioAnalyzer for pooling into sequencing runs. For the first single-cell RNAseq experiment, gene expression and Feature Barcode libraries were pooled and sequenced using the NextSeq 500 with the following cycle parameters: read 1: 26 cycles; i7 index: 8 cycles;

i5 index: 0 cycles; read 2 98 cycles. TCR library was sequenced using NextSeq 500 mid output 2x150: read 1: 150 cycles, i7 index: 8 cycles, and read 2: 150 cycles. This sequencing was performed at the University of Pittsburgh Genomics Research Core.

Generation of filtered gene and barcode matrices and scTCR sequences for scRNAseq

Demultiplexed FASTQ files were generated from raw sequencing data using bcl2fastq (v 2.20.2). CellRanger (10X Genomics; v3.1.0) was used to align demultiplexed reads to the mm10 mouse reference genome to create filtered gene/barcode matrices for downstream analysis. CellRanger was also used to generate consensus TCR alpha and beta sequences for each cell using the "vdj" command. Briefly, consensus TCR sequences per unique cell barcode are generated by first forming a De Bruijn graph and then simplifying it with the aid of the mm10 V(D)J reference sequence.

Identifying samples by demultiplexing cell hashes

We performed cell hashing[77] to run multiple samples within the same lane of the 10x single-cell RNAseq chip. For bioinformatics identification of samples, we first utilized the filtered gene/barcode matrix from each sample to identify all cell barcodes present in the dataset. We then used those cell barcodes and the number of cells identified as input into CITE-seq-Count (v1.4.3, https://hoohm.github.io/CITE-seq-Count/#how-to-cite-cite-seq-count). CITE-seq-Count generated a cell barcode and hash-tag matrix, which was then used to identify cells based on co-expression of cell hashes.

Downstream clustering and analysis

After creating filtered feature/barcode matrices using CellRanger, we used the R package Seurat (v3.1.4)[78] with several modifications for analysis in R v3.6.1. First, filtered feature barcode matrices were read into Seurat, gene expression levels were normalized for library size in each cell by multiplying the expression level by the total number of molecules in a given cell and dividing by 10000. Gene expression levels were scaled across cells by subtracting the mean expression level across all cells from the expression in a given cell and dividing by the standard deviation across all cells[79]. Dimensionality was then reduced based on highly variable genes using principal component analysis, and the top principal components were selected heuristically, retaining all the top components until the increase in variance explained by including the next principal component was negligible. Next, we used UMAP[80] to create a 2-dimensional embedding of the cells from the significant principal components, and DeteRministic Annealing Gaussian mixture mOdels for clusteriNg Single-Cell data (DRAGON) was used for clustering[79]. Plots were generated using ggplot2 (v3.3.2[81], tidyverse (v1.3.0[82]), pheatmap (v1.0.12; https://CRAN.R-project.org/package=pheatmap), patchwork (v1.0.0, https://CRAN.R-project.org/package=patchwork), and ggridges (v0.5.1, https://CRAN.R-project.org/package=ggridges).

scTCRseq analysis

After single-cell TCR sequences were associated with cell barcodes using CellRanger vdj, we next filtered TCRs by those that were full-length and productive. We used the TCRβ complementarity-determining region 3 (CDR3) sequences in conjunction with the

cell barcodes to add the TCRb sequences as “metadata” to Seurat objects for downstream analysis. We used unique TCRβ CDR3 sequences to denote individual T cell clones. We evaluated the expression of TCRs across samples and evaluated the clonality and leveraged TCRs for analysis of differentiation as described below.

Pseudotemporal modeling of differentiation

Diffusion pseudotime is a bioinformatic method of assigning a temporal order to differentiating cells[49,50]. To perform diffusion pseudotime modeling, we used the R package “destiny” v2.14.0[50]. To create the diffusion map, we used all genes expressed with a count of at least 3 in a total of at least 10 cells as input using destiny. We identified genes associated with differentiation by fitting a generalized additive model with the diffusion component 1 as the dependent variable and a loess fit of gene expression as the independent variable using the “gam” R package v1.16.1.

GSEA scoring

GSEA was performed using the Broad Institute software (https://www.broadinstitute.org/gsea/index.jsp). Enrichment scores were calculated by using gene expression counts as input from RNAseq and a gene signature from GSE122713[26] which were created by comparing progenitor and terminally exhausted $CD8^+$ T cells from tumors.

Protein interactome network analysis

We combined context-specific gene expression signatures with HINT[51] (a database of high-quality interactomes in human and several other model organisms) to define context-specific protein subnetworks. We started with expression signatures characterizing intra-islet Cre Control $CD8^+$ T cells and *Lag3*$^{\Delta TM}$ cells and identified direct interactors of the proteins encoded by these seed genes using the murine binary and co-complex interactomes from HINT. For the Cre Control $CD8^+$ T cells and the *Lag3*$^{\Delta TM}$ cells, we used the top 100 differentially expressed genes (50 in each cluster) that were also significantly over-represented in known MSigDB[63] immunological gene signatures involving $CD8^+$ T cells. The subnetworks thus comprised the context-specific seed genes and their direct protein interactors. HINT uses previously established criteria[52] to combine literature-curated and high-throughput interaction datasets. As such, each edge in the corresponding protein interaction network is based on multiple lines of experimental evidence[51]. Sub-network visualizations and network topological analyses were performed using Cytoscape[83].

Over-representation analysis

Over-representation analyses (ORA) were used to determine if gene expression signatures corresponding to 1) intra-islet Cre Control CD8 T^+ cells and 2) *Lag3*$^{\Delta TM}$ cells were enriched in KEGG[44–46] or C7 pathways[63]. Using the top 100 differentially expressed genes (DEGs) in each case (50 from each cluster), we performed ORA via the Webgestalt tool[42,43]. ORA uses a hypergeometric test to evaluate if an input set of genes is over-represented in a pathway, considering jointly the size of the input gene set and the number of genes in the pathway. We reported the top 10 enriched pathways in each case (FDR < 0.05 in all cases).

Statistical Analyses

Data from multiple experiments were pooled for statistical analyses using Prism Version 7 and 8 (GraphPad). The log-rank test was applied to Kaplan-Meier survival function estimates to determine the statistical significance of differences in diabetes incidence between experimental groups. A two-sided nonparametric Mann-Whitney test was used in most other instances, unless otherwise noted. The Non-parametric, unpaired, Mann-Whitney U test is appropriate in the NOD model to compare 2 individual test populations using the median (opposed to a T test which uses the mean) because the data are assumed not normally distributed (ie. ~20% of WT Female NOD mice will never become diabetic). For this reason, the data distribution was assumed to be not normally distributed, but this was not formally tested. Therefore, data met the assumptions of the statistical tests used. A two-sided Pearson's correlation was used to quantify relationships between continuous variables. All tests and P values reported are two sided where P = * <0.05, ** < 0.01, *** < 0.001, **** < 0.0001 and exact P values are reported in figure legends.

Code Availability

Standard R packages were used for data analysis and generation of figures as described in Methods. Code for previously described custom packages is available at www.GitHub.com/arc85/dragonsc. Specific code to generate figures is available upon request.

Extended Data

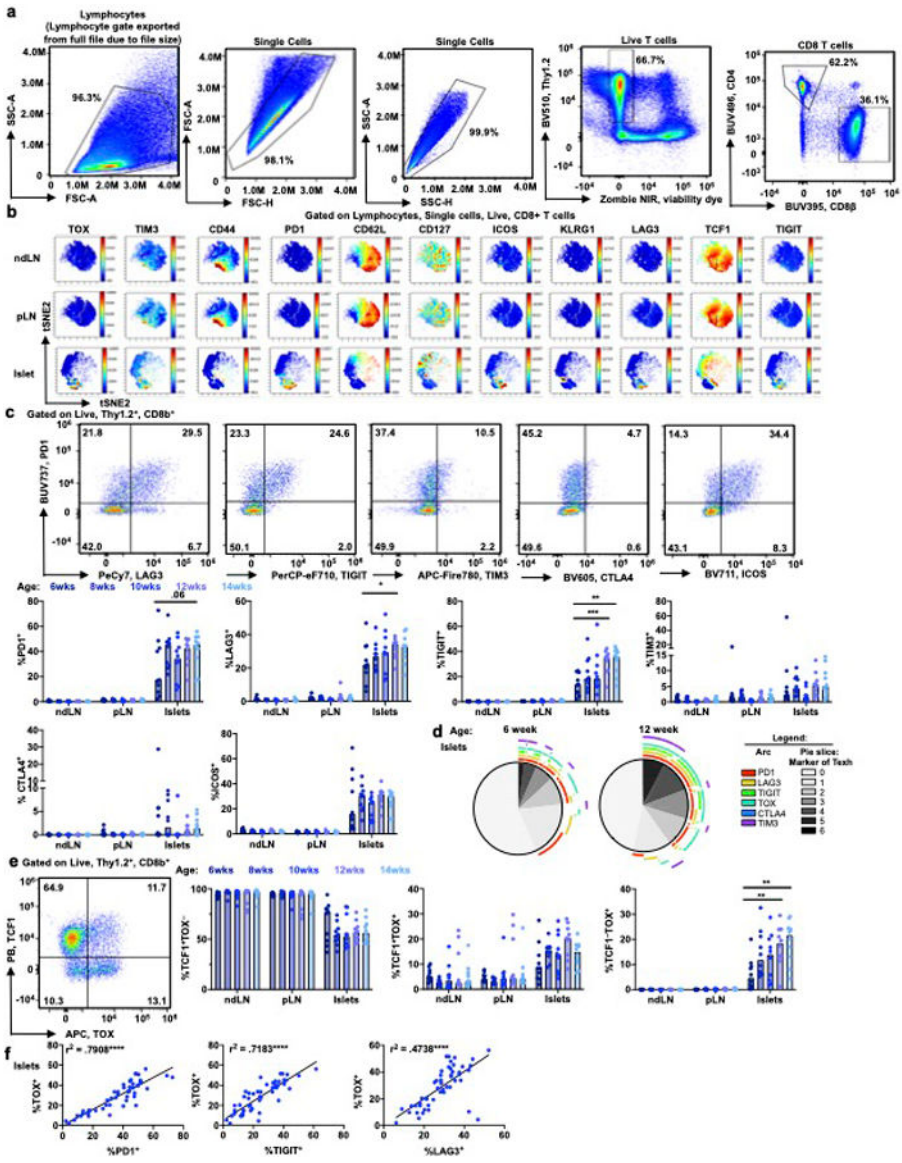

Extended Data Fig. 1. Intra-Islet CD8$^+$ T cells upregulate markers of exhaustion but are a heterogeneous population.

Phenotypic quantification of exhaustion markers in the NOD model of diabetes. (a-f) Spectral flow cytometry for CD8$^+$ T cell functional markers was completed over a time course of 6–14-week-old female WT NOD mice. Representative flow plots are derived from total intra-islet CD8$^+$ T cells (gated on lymphocytes, single cells, Live, Thy1.2$^+$, CD8b$^+$) of 12-week-old female NOD. Data were accumulated from a total of 5 experiments, each experiment had mice of several ages, with n = 10 mice per timepoint, n = 50 total mice. Each point on the graph is representative of a single mouse. (a) Representative flow plotting demonstrating gating strategy to obtain CD8$^+$ T cells. (b) High dimensional analysis at 12 weeks of age was preformed using Cytobank[38] viSNE map analysis (Methods). viSNE maps are shown portraying the 11 markers are used to create FlowSOM clustering analysis.

(c) Representative flow plots of intra-islet CD8$^+$ T cell PD1 and LAG3 (6 vs 12 weeks p=.0355), TIGIT (6 vs 12, 14 weeks p=.0005, .0011), TIM3, CTLA4, and ICOS expression are shown islets and expression of IRs are quantified from the ndLN, pLN, and islets. (d) Co-expression of multiple IRs and the transcription factor TOX are represented in Simplified Presentation of Incredibly Complex Evaluations (SPICE)[71] plots showing bulk CD8$^+$ T cells from 6- and 12-week-old islet samples. (e) Representative flow plots and quantification of bulk intra-islet CD8$^+$ T cell expression of TCF1 and TOX populations. (TCF1–TOX+ 6 vs 12, 14 weeks, p=0.0029, 0.0021) (f) % TOX$^+$ correlation to PD1 (p<.0001), TIGIT (p<.0001), and LAG3 (p<.0001). Pearson's correlation coefficients and r^2 values were calculated. (c and e) A two-sided nonparametric Mann-Whitney was preformed. Graphs portray the median. P = * <0.05, ** < 0.01, *** < 0.001, **** < 0.0001. Unlabeled indicates not statistically significant.

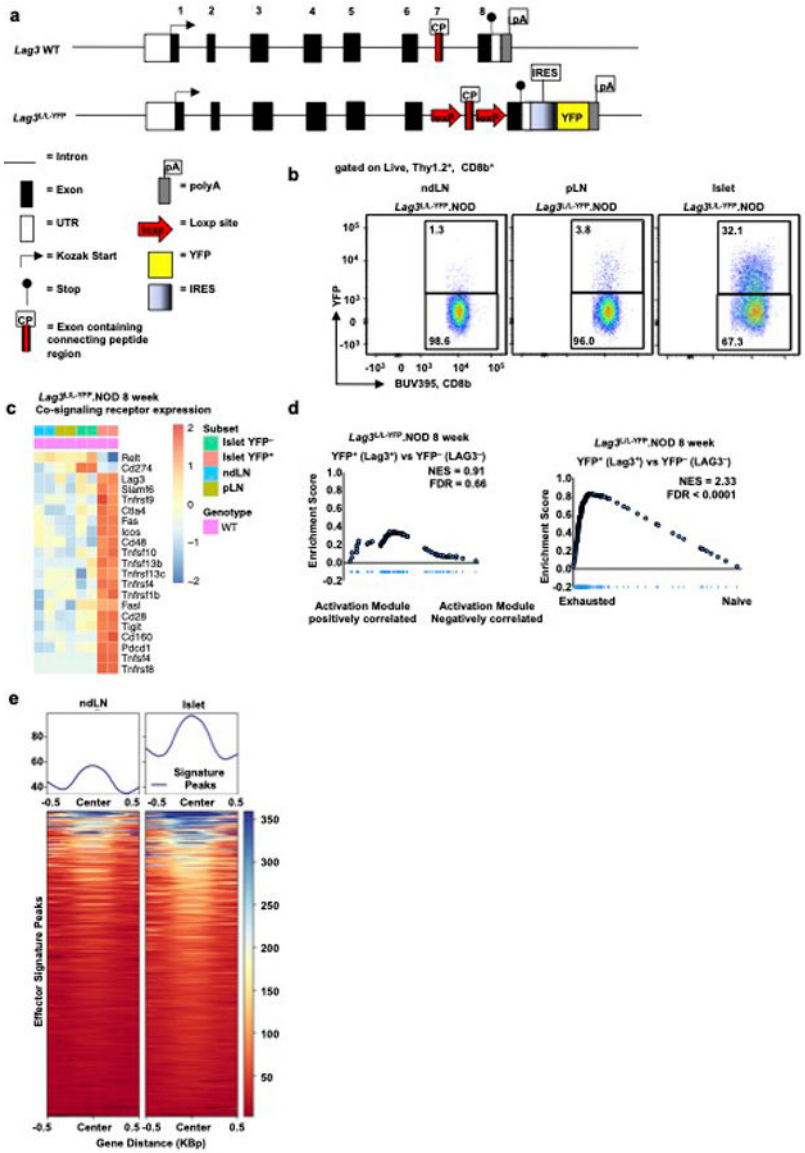

Extended Data Fig. 2. Intra-islet CD8$^+$ T cells express LAG3, which marks exhausted CD8$^+$ T cells, though total intra-islet CD8$^+$ T cells also share features of effector T cells.

Transcriptional and epigenetic analysis was performed on intra-islet CD8$^+$ T cells (a) WT *Lag3* locus is shown in the top panel. The *Lag3*$^{L/L\text{-}YFP}$ construct is generated by inserting LoxP sites flanking the transmembrane region, exon 7, of the *Lag3* gene (middle panel). (b) YFP expression is demonstrated in the *Lag3*$^{L/L\text{-}YFP}$.NOD, marking those CD8$^+$ T cells which have transcribed *Lag3*. (c-d) Bulk population RNAseq was preformed comparing intra-islet YFP$^+$ and YFP$^-$ CD8$^+$ T cells, along with YFP$^-$ ndLN and pLN controls. Cells are pooled from 3 *Lag3*$^{L/L\text{-}YFP}$.NOD 8 week old females in 2 independent experiments. (c) Relative expression of selected co-stimulatory or co-inhibitory receptors in the YFP$^+$ vs YFP$^-$ intra-islet CD8$^+$ T cells. (d) Leading-edge gene set enrichment analysis was preformed comparing YFP$^+$ and YFP$^-$ intra-islet CD8$^+$ T cells to published exhaustion[72] and activation[73] datasets. NES = Normalized Enrichment score, fdr = false discovery rate. (Methods) (e) scATACseq was preformed comparing E8i$^{CRE/CRE\text{-}GFP}$.NOD CD8$^+$ T cells derived from islets and ndLN (n = 4, 8 week Females). Enrichment for effector signature peaks is shown.

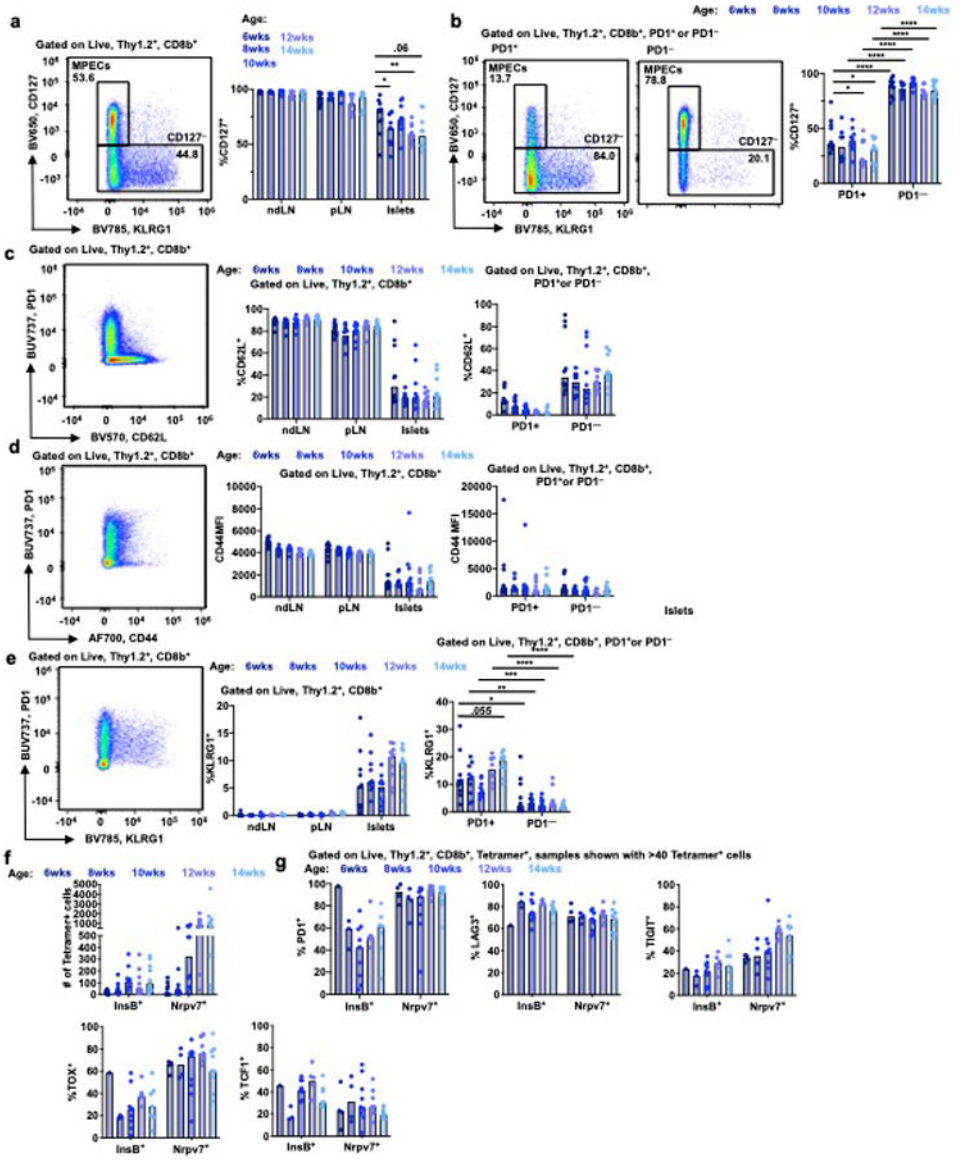

Extended Data Fig. 3. ~50% of intra-islet CD8$^+$ T cells express markers of memory, while only a small fraction express marker of naivety or effector function, while Tetramer$^+$ cells have minimal changes in phenotype with disease progression.

Flow cytometric quantification of markers associated with naïve, effector, and memory CD8$^+$ T cell subsets. (a-g) Spectral flow cytometry for CD8$^+$ T cell functional markers was completed over a timecourse of 6–14-week-old female WT NOD mice. Representative flow plots are derived from total intra-islet CD8$^+$ T cells (gated on lymphocytes, single cells, Live, Thy1.2$^+$, CD8b$^+$) of 12-week-old female NOD. Data were accumulated from a total of 5 experiments, each experiment had mice of several ages with n = 10 mice per timepoint, n = 50 total mice. Each point on the graph is representative of a single mouse. Data shown is analyzing total intra-islet CD8$^+$ T cells, gated on Live, Thy1.2$^+$, CD8b$^+$ or PD1$^+$ vs PD1$^-$ intra-islet CD8$^+$ T cells. (a) Representative flow plot and quantification of CD127 expression on total ndLN, pLN and intra-islet CD8$^+$ T cells (6 vs. 8, 12, 14 weeks, p=.0288, .0089, .063) (b) Representative flow plot and quantification of CD127 expression

on or PD1$^+$ vs PD1$^-$ intra-islet CD8$^+$ T cells (PD1$^+$ vs PD1$^-$ p<.000001 at all time points, 6 vs 12, 14 weeks PD1$^+$ p=.05, .05). (c) Quantification of CD62L in islets compared to ndLN and pLN, as well as on intra-islet PD1$^+$ vs PD1$^-$ populations. (d) Representative flow plot and MFI of CD44 expression on ndLN, pLN, islet, and islet PD1 subsets. (e) Representative flow plot of KLRG1 expression and quantification of KLRG1 on ndLN, pLN, islet, and islet PD1 subsets (PD1$^+$ vs PD1$^-$ 6, 8, 10, 12, 14 weeks p = .0288, .0011, .0003, .000076, .000011, 6 vs 14 weeks PD1$^+$ p=.055). (f) Quantification of tetramer$^+$ CD8$^+$ T cells in the islet's over time. (g) Expression of CD8$^+$ T cell functional markers on tetramer$^+$ populations in the islets. Only samples consisting of >40 Tetramer$^+$ CD8$^+$ T cells are shown. Tetramer staining in lymph nodes was negligible and never exceeded 40 tetramer$^+$ cells. (a-g) Each data point corresponds to a single mouse. A two-sided nonparametric Mann-Whitney was preformed, where P = * <0.05, ** < 0.01, *** < 0.001, **** < 0.0001. Unlabeled indicates not statistically significant. Graphs portray the median.

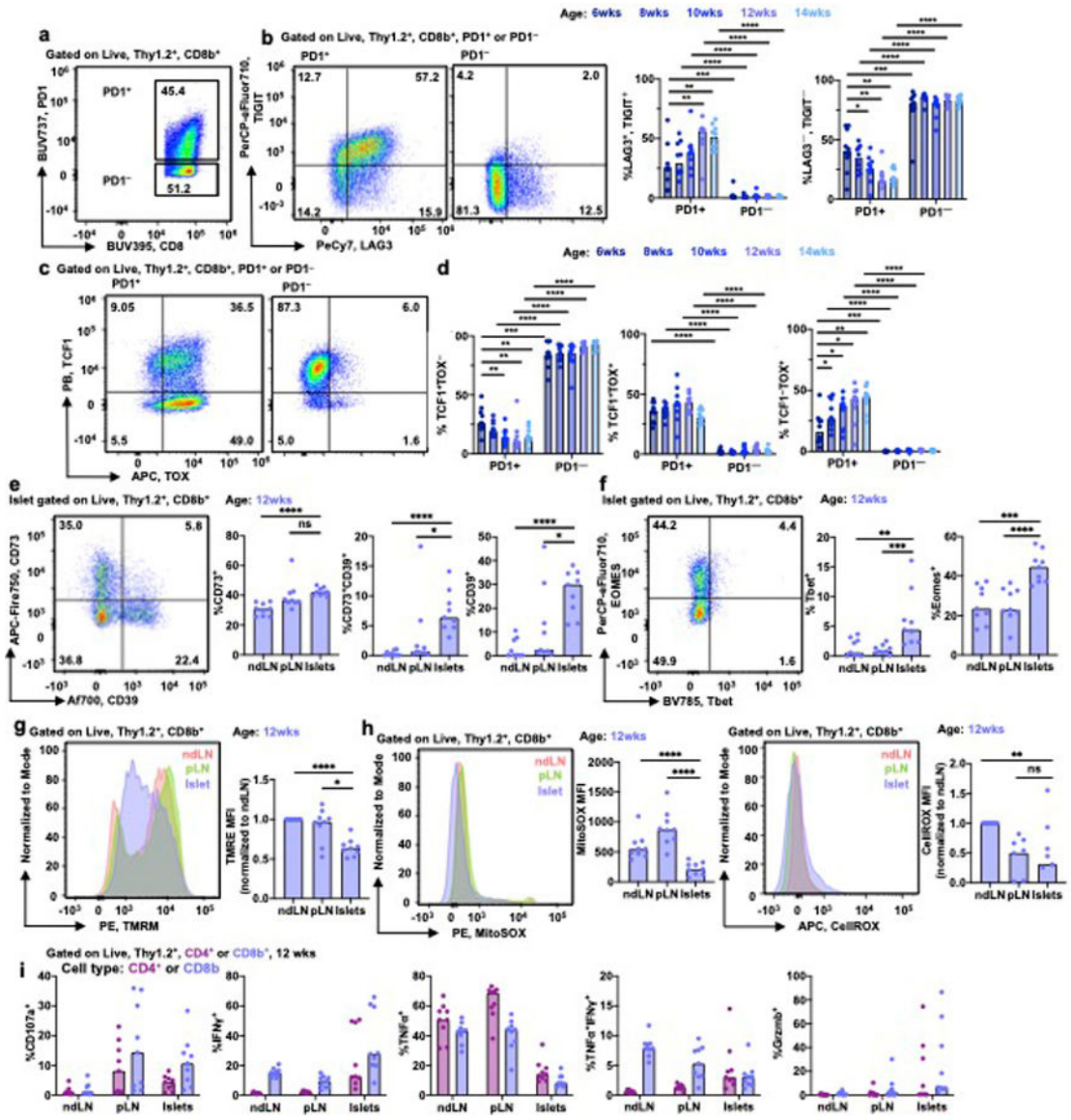

Extended Data Fig. 4. A subset of intra islet CD8$^+$ T cells upregulate markers of exhaustion, as well as effector cell markers.

(a-d) Spectral flow cytometry for CD8$^+$ T cell functional markers was completed and representative flow plots and graphs appear as described in Extended Data Figure 1, with the added sub gate of PD1$^+$ and PD1$^-$. (a) representative flow plot of intra-islet CD8$^+$ T cells PD1 expression. (b) Representative flow plots and quantification of LAG3 and TIGIT expression on PD1$^+$ and PD1$^-$ intra-islet CD8$^+$ T cells. (LAG3$^+$TIGIT$^+$: PD1$^+$ vs PD1$^-$ 6, 8, 10–14 weeks p=.0005, .000002, <.000001, 6 vs 12, 14 weeks PD1$^+$ p=.0039, .0065. LAG3$^-$TIGIT$^-$: PD1$^+$ vs PD1$^-$ 6, 8–14 weeks p=.000174, <.000001, 6 vs 10, 12, 14 weeks PD1$^+$ p=.028, .006, .005). (c) Representative flow plots of TCF1 and TOX staining on PD1$^+$ and PD1$^-$ intra-islet CD8$^+$ T cells. (d) quantification of (c) (TCF1$^+$TOX$^-$: PD1$^+$ vs PD1$^-$ p=.000011 at all time points, 6 vs 10, 12, 14 weeks PD1$^+$ p=.0027, .0019, .0064. TCF1$^+$TOX$^+$: PD1$^+$ vs PD1$^-$ p=<.000001 at all timepoints. TCF1$^-$TOX$^+$: PD1$^+$ vs PD1$^-$ 6, 8–14 weeks p=.000262, <.000001, 6 vs 8, 10, 12, 14 weeks p=.0355, .0355, .0147,

.0014). (e-f) Total intra-islet $CD8^+$ T cells from 12-week-old female WT NOD mice were analyzed by spectral flow cytometry including ndLN and pLN controls (n=10, 2 independent experiments). (e) Representative flow plots (islets) and quantification of CD73 and CD39 expression ($CD73^+$: islets vs ndLN, pLN p=<.0001, .06. $CD39^+CD73^+$: islets vs ndLN, pLN, p=<.0001, .0142. $CD39^+$: islets vs ndLN, pLN, p=<.0001, .0315). (f) Representative flow plots (islets) and quantification of Tbet and Eomes expression ($Tbet^+$: islets vs ndLN, pLN, p=.0056, .0003. $Eomes^+$: islets vs ndLN, pLN, p=.0005, <.0001). (g-i) intra-islet $CD8^+$ T cells were isolated and from 12-week-old female WT NODs and analyzed by flow cytometry for metabolic markers or cytokines (n = 10, 2 independent experiments, techniques described in methods) (g) intra-islet $CD8^+$ T cells are stained for TMRM (islets vs ndLN, pLN p=<.0001, .0106), (h) MitoSOX (islets vs. ndLN and pLN, p<.0001) and CellROX (islets vs ndLN p=.0019), and for (i) cytokine production. (a-i) Each data point corresponds to a single mouse. A two-sided nonparametric Mann-Whitney was preformed, where P = * <0.05, ** < 0.01, *** < 0.001, **** < 0.0001. Unlabeled indicates not statistically significant. Graphs portray the median.

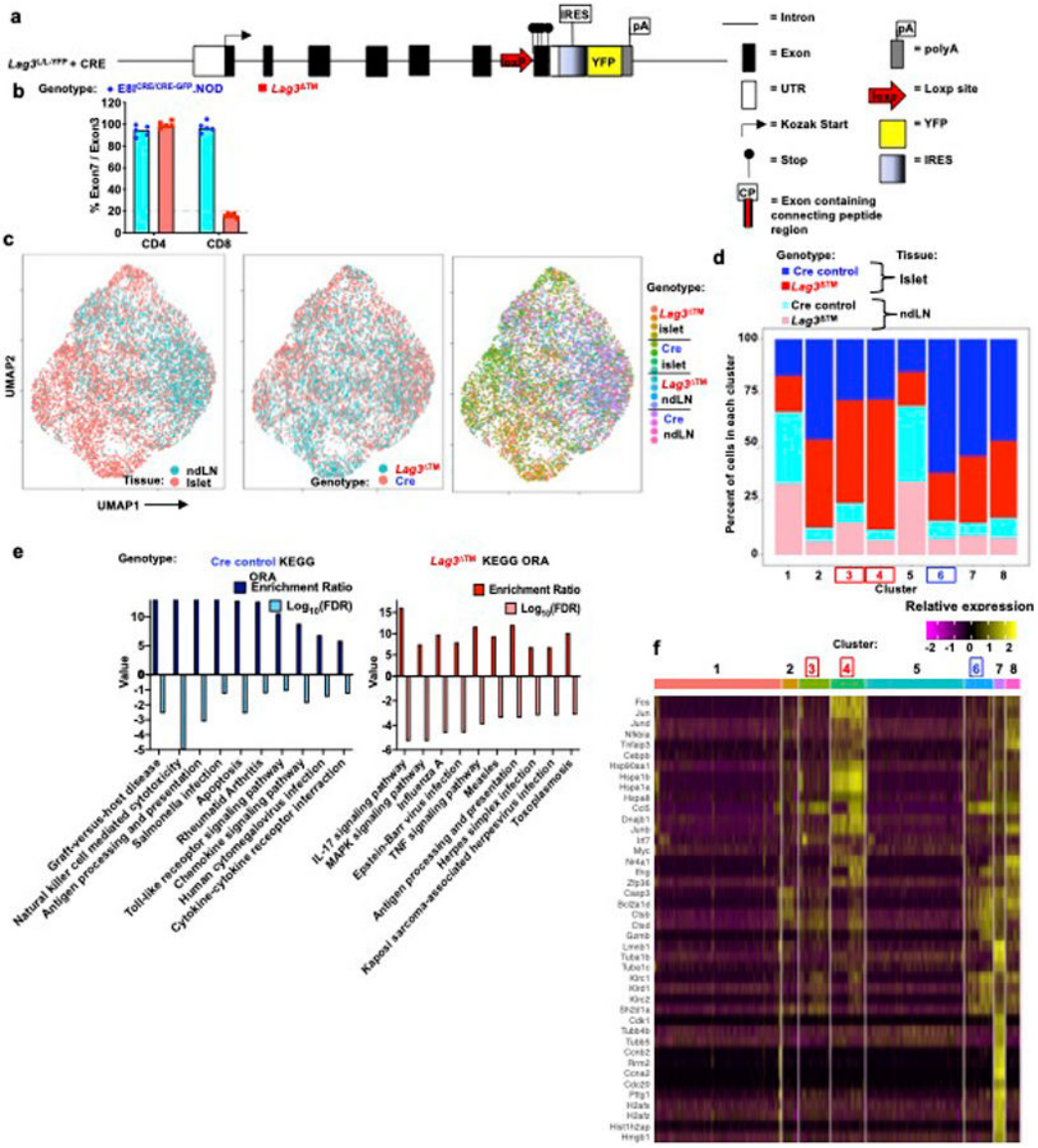

Extended Data Fig. 5. scRNAseq reveals transcriptionally unique clusters and functions of Cre Control versus *Lag3*$^{\Delta TM}$ CD8^{+} T cells.

scRNAseq assessment of intra-islet CD8^{+} T cells. (a) The *Lag3*$^{L/L\text{-}YFP}$ (Extended Data Fig. 2a) construct crossed to a Cre recombinase is shown. Upon crossing *Lag3*$^{L/L\text{-}YFP}$ to a Cre recombinase, exon 7 (the transmembrane domain) is deleted (*Lag3*$^{\Delta TM}$). The result is the generation of only the soluble form of LAG3 protein. (b) qPCR determining deletion efficiency of the CD8 specific LAG3$^{\Delta TM}$ mouse. Ratio of Exon 7 to Exon 3 was quantified in Cre Control (E8I$^{CRE/CRE\text{-}GFP}$.NOD), vs *Lag3*$^{\Delta TM}$ (*Lag3*$^{L/L\text{-}YFP}$E8I$^{CRE/CRE\text{-}GFP}$.NOD) experimental mice. Cells derived from spleens of five 8-week-old females for 1 experiment (n = 5). (c-g) CD8^{+} T cells from the islets and ndLN were isolated from 4 Cre Control and 4 *Lag3*$^{\Delta TM}$ 8-week-old NOD female mice and were subjected to 5' paired single cell RNAseq (scRNAseq) and single cell T cell receptor sequencing (scTCRseq). (c) Cells were visualized by UMAP and colored by tissue, genotype, or individual sample. (d) Quantification of specific cell types in each DRAGON cluster (Fig. 3b). (e)

Overrepresentation analyses on gene signatures characterizing the Cre Control (6) and *Lag3*$^{\Delta TM}$ dominated clusters (3+4) was performed using KEGG pathways and the top 10 overrepresented in each genotype are shown. Enrichment ratio and –$\log_{10}$FDR (false discovery rate) are portrayed. (f) Heatmap of gene expression levels in the over-represented KEGG pathways.

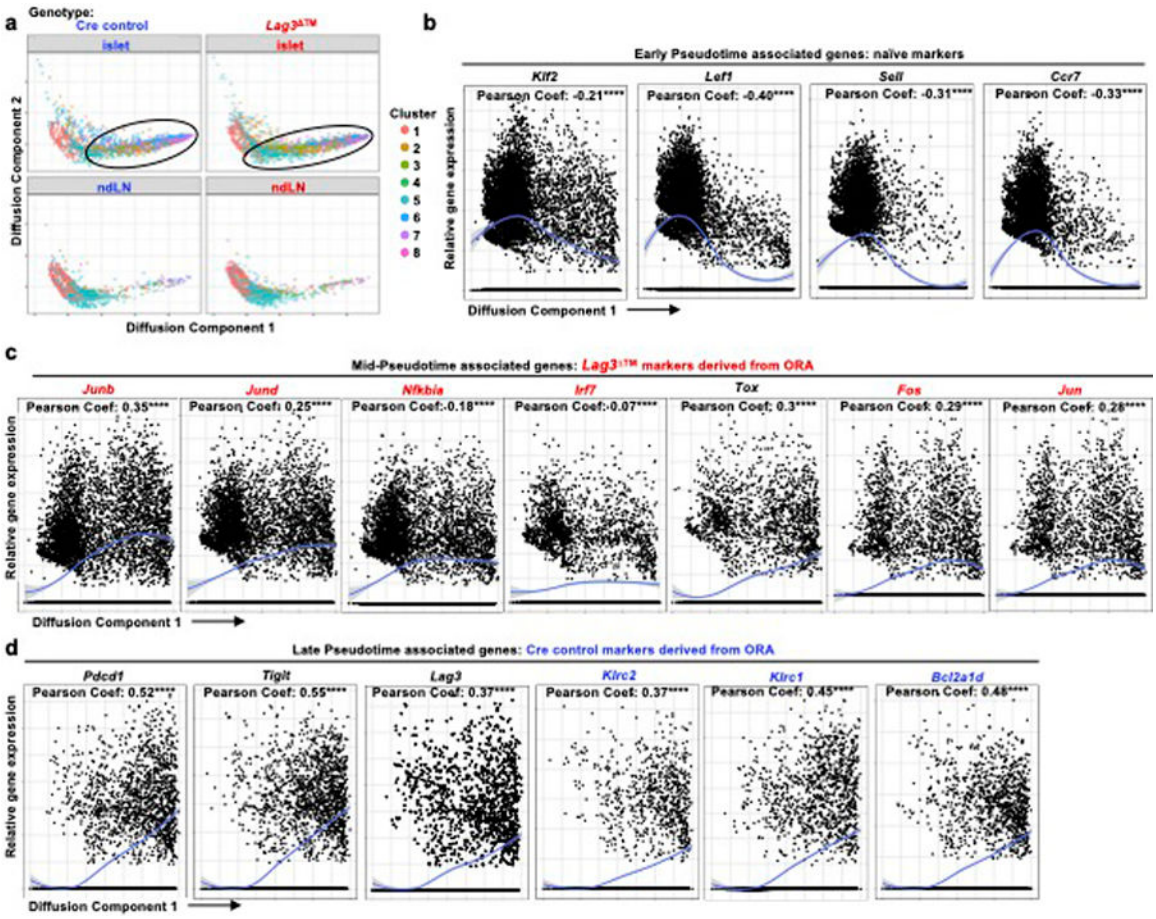

Extended Data Fig. 6. Pseudotemporal analysis recapitulates the development of exhaustion in intra-islet CD8$^+$ T cells and reveals key differences between *Lag3*$^{\Delta TM}$ and Cre Controls.

Diffusion maps were constructed and pseudotemporal ordering was inferred (Methods) using single-cell RNAseq data described in Ext. Data Fig. 5. (a-d) CD8$^+$ T cells from the islets and ndLN were isolated from 4 Cre Control and 4 *Lag3*$^{\Delta TM}$ 8-week NOD female mice and were subjected to 5' paired single cell RNAseq (scRNAseq) and single cell T cell receptor sequencing (scTCRseq). Unless otherwise noted, red is representative of *Lag3*$^{\Delta TM}$ dominated clusters (3+4) and blue is representative of Cre Control dominated clusters (6). Diffusion component 1 and 2 portray the trajectory of CD8$^+$ T cell differentiation. (a) Diffusion pseudotime colored by DRAGON cluster (Fig. 3b). (b-d) Differential gene expression as a function of diffusion pseudotime. Genes associated with early pseudotime (b), mid-pseudotime (c), and late pseudotime (d). Red corresponds to ORA markers of *Lag3*$^{\Delta TM}$ dominated clusters and blue is representative of Cre Control dominated cluster

markers derived from ORA analysis. Two sided Pearson's correlation was used to calculated the Pearson's correlation coefficient where P <2.2x10^{-16} (indicated as ****) in all cases.

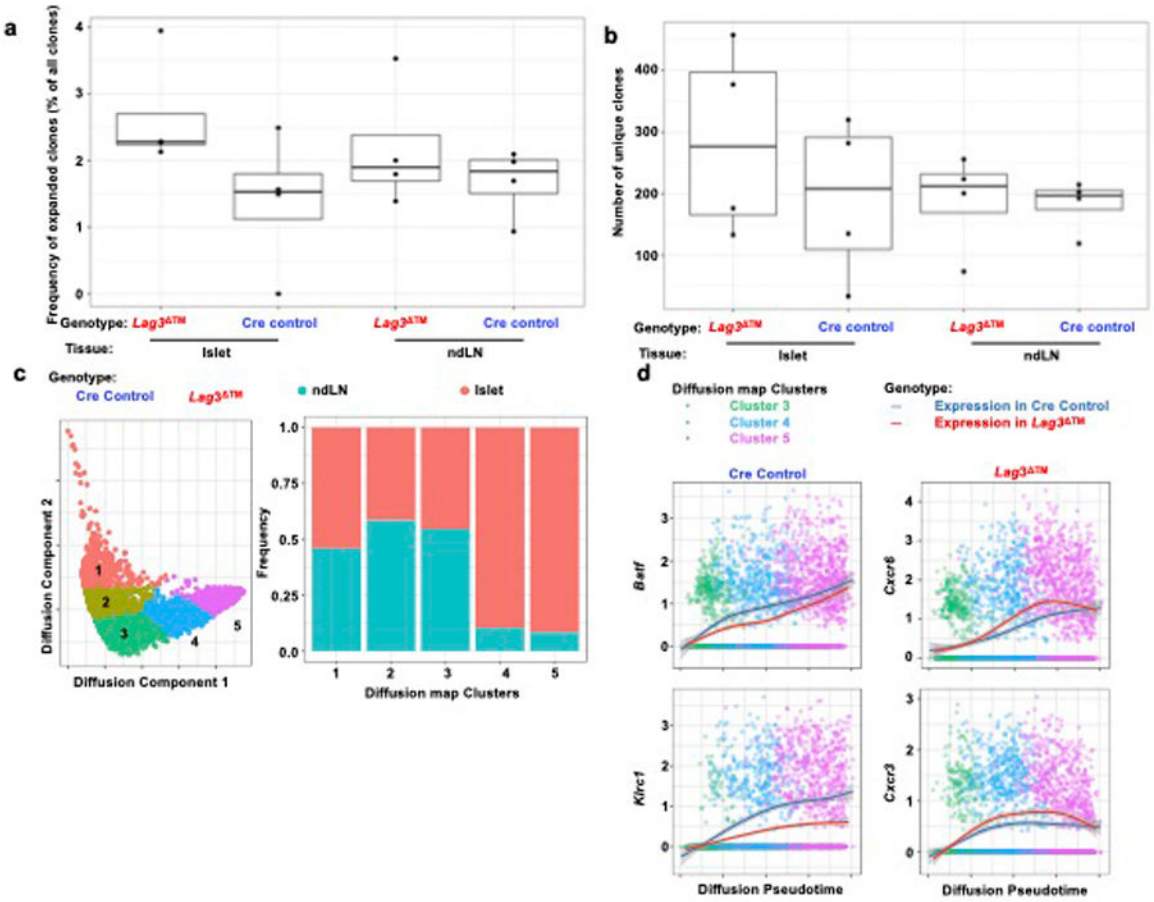

Extended Data Fig. 7. TCR clonality in conjunction with diffusion pseudotime distinguish *Lag3*$^{\Delta TM}$ and Cre Control samples.

(a-d) CD8+ T cells from the islets and ndLN were isolated from 4 Cre Control and 4 Lag3ΔTM 8-week NOD female mice and were subjected to 5' paired single cell RNAseq (scRNAseq) and single cell T cell receptor sequencing (scTCRseq). Red is representative of Lag3ΔTM dominated clusters (3+4) and blue is representative of Cre Control dominated clusters (6). (a-b) 5' scTCRseq was analyzed for frequency of expanded clones (a) and number of unique clones (b). Here, the line is the median, box is lower and upper quantiles (lower 25% and upper 25%), the upper whisker is the minimum of either the maximum value or the upper quartile plus 1.5 times the interquartile ranger. Bottom whisker is the maximum of the minimum or the first quartile minus 1.5 times in interquartile ranger. (c-d) Diffusion component 1 and 2 portray the trajectory of cellular development. (c) Diffusion pseudotime trajectory was divided into 5 clusters based on DC1 and DC2. Enrichment for islets begins in cluster 3, and clusters 4 and 5 constitute ˜90% of cells derived from islets. (d) Expression of genes differentially regulated over time between Cre Control and Lag3ΔTM in clusters enriched for cells derived from islet (i.e. clusters 3, 4 and 5).

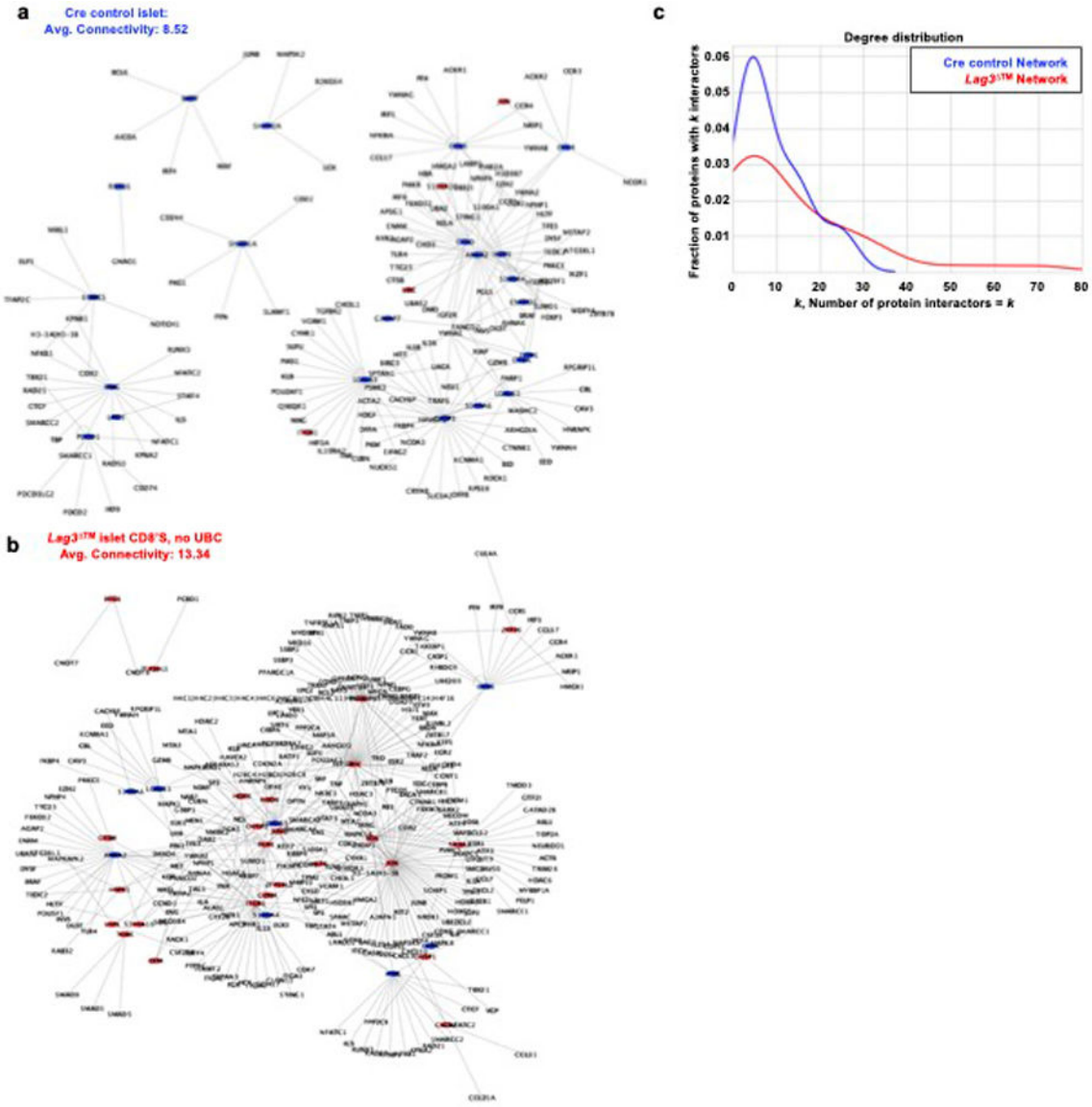

Extended Data Fig. 8. Network analysis reveals differences in possible interactions between *Lag3*$^{\Delta TM}$ and Cre Control

(a-c) CD8^{+} T cells from the islets and ndLN were isolated from 4 Cre Control and 4 *Lag3*$^{\Delta TM}$ 8-week NOD female mice and were subjected to 5' paired single cell RNAseq (scRNAseq) and single cell T cell receptor sequencing (scTCRseq). Unless otherwise noted, red is representative of *Lag3*$^{\Delta TM}$ seed genes (Clusters 3+4) and blue is representative of Cre Control seed genes (Cluster 6) (Supplementary Table 4). For subnetworks, all gene names are shown. (a) Protein subnetworks characterizing Cre Control (b) Protein subnetworks characterizing *Lag3*$^{\Delta TM}$ cells (c) Degree distribution for the different subnetworks showing that Cre Control have a higher frequency of networks with fewer connections

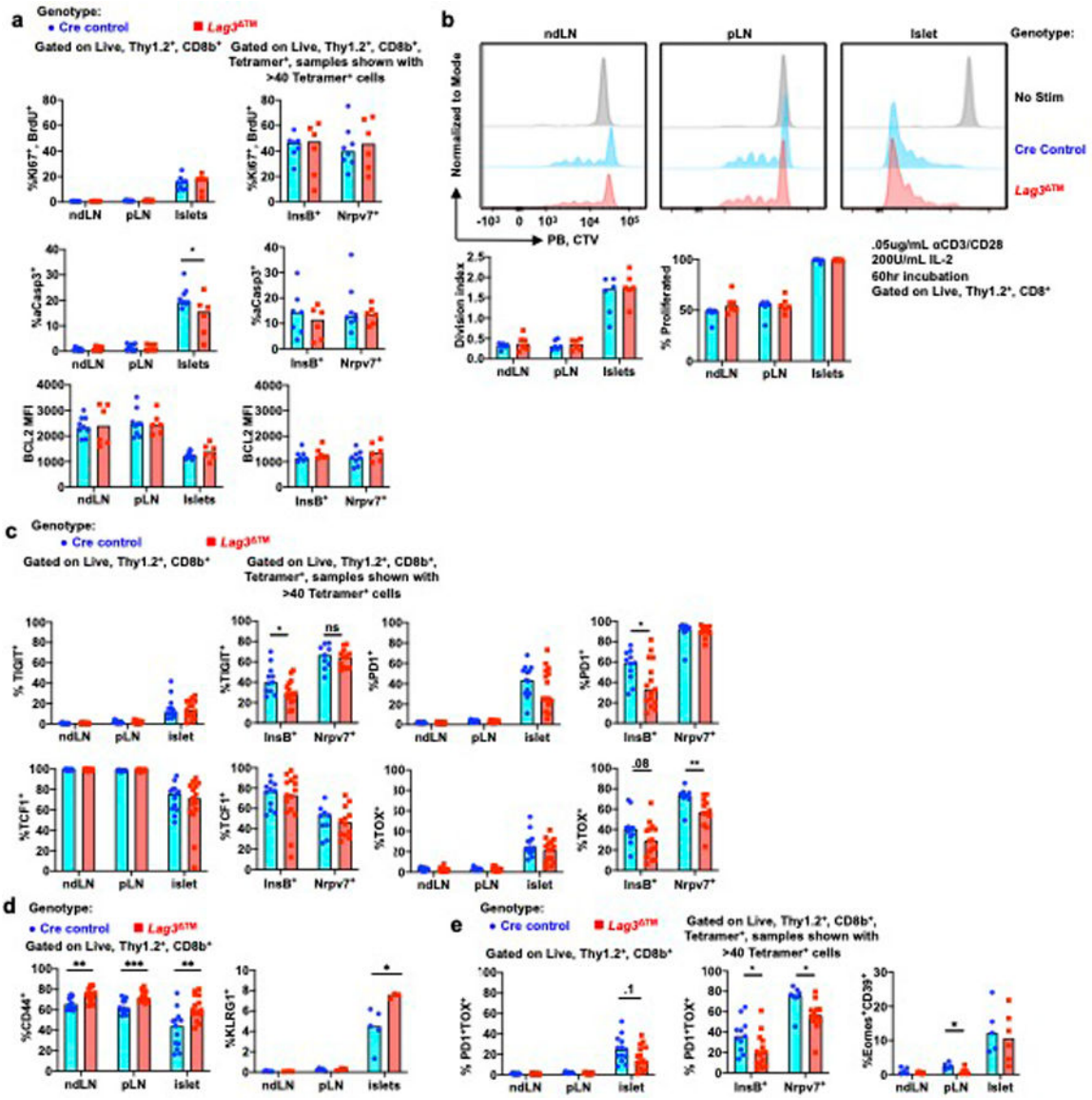

Extended Data Fig. 9. LAG3 deletion has moderate impacts on proliferation, but phenotypically skews cells to an effector, rather than restrained phenotype.

The consequences of LAG3 deletion were evaluated by flow cytometry to phenotype intra-islet CD8+ T cells for survival, proliferation, and IR/exhaustion related marker expression. (a-e) Flow cytometry was performed on 8-week-old female Lag3ΔTM and Cre Controls taking cells from ndLN, pLN and islets. Data points derived from islets having <40 tetramer+ cells were excluded. Tetramer staining in lymph nodes was negligible and never exceeded 40 Tetramer+ cells. (a) BrdU was injected intraperitoneally 12 hours prior to harvest, and percent BrdU, Ki67, cleaved Caspase 3 (p=.0496), and BCL2 were assessed by flow cytometry (2 independent experiments, n = 6–8 per genotype). (b) CD8+ T cells were labeled with cell trace violet, sorted into 96 well round bottom plate containing 0.05 ug/mL αCD3/CD28, and 200U/mL IL-2 in cRPMI, and cultured for 60 hours and analyzed by flow cytometry (2 independent experiments, n = 6 per genotype). (c) IRs/markers of restraint (TIGIT, TCF1, PD1, and TOX) expression were quantified on total and tetramer

positive CD8+ T cells (3 independent experiments, n =13–15 per genotype Tetramer: TIGIT, PD1, TOX, p=.0473, .0473, .0096). (d) Percent expression of effector molecules CD44 (3 independent experiments, n = 13–15 per genotype ndLN, pLN, Islets p=.0016, .0007 .0037) and KLRG1 (1 independent experiment, n = 4–5 per genotype p=.036). (e) Percent expression of PD1 and TOX (Nrpv7+ p=.0259, InsB+ p=.0204), CD39 and Eomes (p=.03), double positive populations, markers of exhaustion, were monitored on bulk and tetramer positive ndLN, pLN, and intra-islet CD8+ T cells (3 independent experiments, n = 13–15 per genotype and 2 independent experiments, n = 5–6 per genotype, respectively). (a-e) Each data point corresponds to a single mouse. A two-sided nonparametric Mann-Whitney statistical test was preformed where P = * <0.05, ** < 0.01, *** < 0.001, **** < 0.0001. Unlabeled indicates not statistically significant. Graphs portray the median.

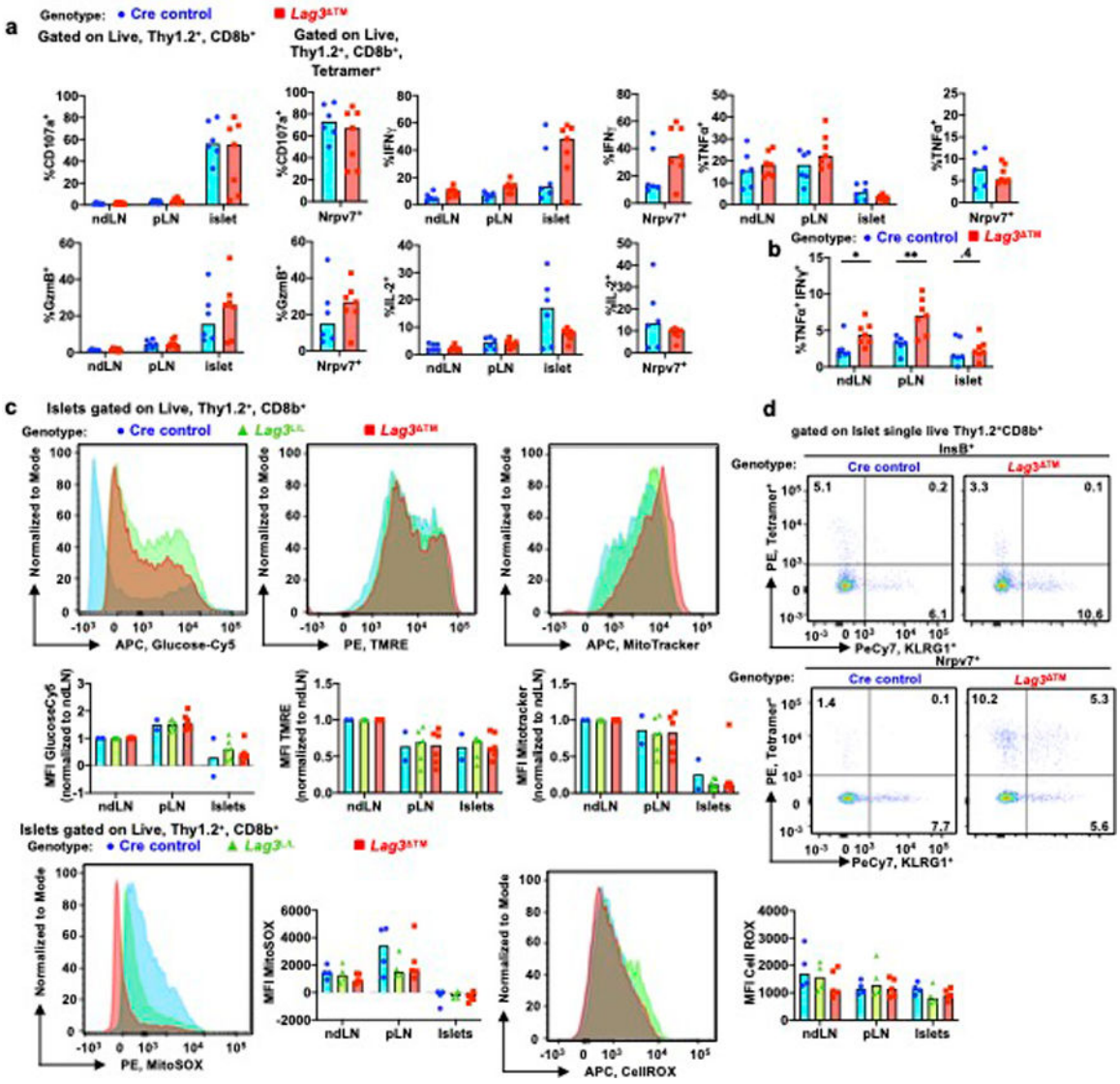

Extended Data Fig. 10. LAG3 deletion doesn't affect single cytokine production or metabolic capacity

The consequences of LAG3 deletion were evaluated by flow cytometry to phenotype intra-islet CD8$^+$ T cells for cytokine production, metabolic capacity, and antigen specificity. (a-d) Flow cytometry was performed on 8-week-old female *Lag3*$^{\Delta TM}$ and Cre Controls taking cells from ndLN, pLN and islets. (a-b) lymphocytes were stimulated *ex vivo* for 5 hours with PMA, ionomycin, and brefeldin A and then assessed for cytokine production and degranulation. CD107a, GzmB, Tnfα and IFNγ were quantified (2 independent experiments n = 6–7 per genotype). Cytokine production is unchanged between genotypes, though dual cytokine production, an indicator of polyfunctionality, IFNγ$^+$Gzmb$^+$, is increased in *Lag3*$^{\Delta TM}$ (ndLN, pLN, Islet p=.0083, .035, .44) (b). (c) Lymphocytes were isolated from islets, ndLN, and pLN, cultured in serum free media for 37 degrees C in the presence of GlucoseCy5, CellROX, or MitoSOX, for 30 mins, surface stained including TMRE and MitoTracker, and analyzed by flow cytometry (2 independent experiments, n=2–6 per genotype). *Lag3*$^{L/L\text{-}YFP}$.NOD controls were included in this experiment to control for fluorescent protein expression that may overlap with metabolic markers. (a-c) Each data point corresponds to a single mouse. A two-sided nonparametric Mann-Whitney statistical test was preformed where P = * <0.05, ** < 0.01, *** < 0.001, **** < 0.0001. Unlabeled indicates not statistically significant. Graphs portray the median. (d) representative flow plots of tetramer staining in 8-week-old female *Lag3*$^{\Delta TM}$ and Cre Controls intra-islet CD8$^+$ T cells.

Supplementary Material

Refer to Web version on PubMed Central for supplementary material.

Acknowledgements

We wish to thank all the current and former members in the Vignali Lab (Vignali-lab.com; @Vignali_Lab) for all their constructive comments and advice during this project. The authors also wish to thank all the members of P01 AI108545 for their constructive feedback, specifically Arlene Sharpe and members of her lab (Department of Microbiology and Immunobiology, Harvard Medical School, Boston, MA, USA). We thank Greg Delgoffe and members of his lab for aid in metabolic studies and protocols (Department of Immunology, University of Pittsburgh, Pittsburgh, PA, USA, Tumor Microenvironment Center, UPMC Hillman Cancer Center, Pittsburgh, PA, USA, Cancer Immunology and Immunotherapy Program, UPMC Hillman Cancer Center, Pittsburgh, PA, USA). We also thank Qian Zhan for help with histology (Department of Pathology, Brigham and Women's Hospital and Harvard Medical School, Boston, MA, USA). We thank R. Dadey, H. Yano, L. Andrews, R. Peralta, and P. Vignali, members of the Vignali and Delgoffe labs, for aid in unpublished experiments. We thank D. Falkner, A. McIntyre, N. Sheng, H. Gunzelman, T. Sturgeon, H. Shen and L. Borghesi from the Immunology Flow Core (current and past) for cell sorting, maintenance and training in the use of cytometers (Department of Immunology, University of Pittsburgh School of Medicine, Pittsburgh, PA, USA). We thank J. Goulet, R. Gerheart, C. Schmidt, J. Latini and the staff of the Division of Laboratory Animals for genotyping and animal husbandry (Department of Immunology, University of Pittsburgh School of Medicine, Pittsburgh, PA, USA). We thank the Littman (The Kimmel Center for Biology and Medicine of the Skirball Institute, New York University School of Medicine, New York, NY USA, Howard Hughes Medical Institute, New York, NY, USA) and Taniuchi (Laboratory for Transcriptional Regulation, RIKEN Center for Integrative Medical Sciences (IMS), 1–7-22 Suehiro-cho, Tsurumi-ku, Yokohama, 230–0045, Japan) labs for the E8i$^{CRE\text{-}GFP}$.C57BL/6 mice and A. Castellaw for breeding them onto the NOD background at St. Jude Children's Research Hospital (Department of Immunology, St. Jude Children's Research Hospital, Memphis, TN, USA). We also thank the UPMC Genome Core and the University of Pittsburgh HSCRF Genomics Research Core for assistance with next-generation sequencing, and the Pitt Center for Research Computing for computational resources. This work was supported by the National Institutes of Health (R01 DK089125, R01 AI144422, P01 AI108545 to D.A.A.V., AI105343, AI117950, AI082630, AI112521, AI115712, AI108545, CA210944 to E.J.W, F31 AI147638 and T32 AI089443 to S.G). E.J.W. is supported by the Parker Institute for Cancer Immunotherapy which supports the cancer immunology program at Upenn. A.R.C. is supported by the Hillman Postdoctoral Fellows for Innovative Cancer Research postdoctoral fellowship. This project benefitted from a SPECIAL ORDER BD LSR FORTESSA™ (funded by NIH S10 OD011925) used in the UPSOM Unified Flow Core.

Data Availability

The following Databases were used for analysis in our manuscript (see Methods for details): Mouse genome for alignment of sequencing data: Genome Reference Consortium Mouse Build 38 (Fig. 1b, 2, Extended Data Fig. 2c–d, 5–7, https://www.ncbi.nlm.nih.gov/assembly/GCF_000001635.20/), HINT – to generate protein protein interaction networks (Extended Data Fig. 8 http://hint.yulab.org/)[51], KEGG (Extended Data Fig. 5e https://www.genome.jp/kegg/)[44–46], C7 Immunologic Signature Gene Sets (Extended Data Fig. 5e, http://www.gsea-msigdb.org/gsea/msigdb/collections.jsp)[63].

The following Datasets were used for analysis in our manuscript: ATACseq (Fig. 1c, Extended Data Fig. 2e GSE86797[64]), Bulk RNAseq GSEA (Extended Data Fig. 2c, GSE41867[65]), scRNAseq GSEA (Fig. 3c, GSE122713[26]).

Sequencing data generated in this manuscript are deposited in Gene Expression Omnibus (GEO) database under the accession code GSE199357.

References

1. Blank CU et al. Defining ‘T cell exhaustion’. Nat Rev Immunol 19, 665–674, doi:10.1038/s41577-019-0221-9 (2019). [PubMed: 31570879]
2. Beltra JC et al. Developmental Relationships of Four Exhausted CD8(+) T Cell Subsets Reveals Underlying Transcriptional and Epigenetic Landscape Control Mechanisms. Immunity 52, 825–841.e828, doi:10.1016/j.immuni.2020.04.014 (2020). [PubMed: 32396847]
3. Khan O et al. TOX transcriptionally and epigenetically programs CD8(+) T cell exhaustion. Nature 571, 211–218, doi:10.1038/s41586-019-1325-x (2019). [PubMed: 31207603]
4. Scott AC et al. TOX is a critical regulator of tumour-specific T cell differentiation. Nature 571, 270–274, doi:10.1038/s41586-019-1324-y (2019). [PubMed: 31207604]
5. Seo H et al. TOX and TOX2 transcription factors cooperate with NR4A transcription factors to impose CD8(+) T cell exhaustion. Proc Natl Acad Sci U S A 116, 12410–12415, doi:10.1073/pnas.1905675116 (2019). [PubMed: 31152140]
6. Yao C et al. Single-cell RNA-seq reveals TOX as a key regulator of CD8(+) T cell persistence in chronic infection. Nat Immunol 20, 890–901, doi:10.1038/s41590-019-0403-4 (2019). [PubMed: 31209400]
7. Tilstra JS et al. Kidney-infiltrating T cells in murine lupus nephritis are metabolically and functionally exhausted. J Clin Invest 128, 4884–4897, doi:10.1172/jci120859 (2018). [PubMed: 30130253]
8. Smita S, Chikina M, Shlomchik MJ & Tilstra JS Heterogeneity and clonality of kidney-infiltrating T cells in murine lupus nephritis. JCI Insight, doi:10.1172/jci.insight.156048 (2022).
9. Long SA et al. Remodeling T cell compartments during anti-CD3 immunotherapy of type 1 diabetes. Cell Immunol 319, 3–9, doi:10.1016/j.cellimm.2017.07.007 (2017). [PubMed: 28844471]
10. McKinney EF, Lee JC, Jayne DR, Lyons PA & Smith KG T-cell exhaustion, co-stimulation and clinical outcome in autoimmunity and infection. Nature 523, 612–616, doi:10.1038/nature14468 (2015). [PubMed: 26123020]
11. Wiedeman AE et al. Autoreactive CD8+ T cell exhaustion distinguishes subjects with slow type 1 diabetes progression. J Clin Invest 130, 480–490, doi:10.1172/jci126595 (2020). [PubMed: 31815738]
12. Long SA et al. Partial exhaustion of CD8 T cells and clinical response to teplizumab in new-onset type 1 diabetes. Sci Immunol 1, doi:10.1126/sciimmunol.aai7793 (2016).
13. Pauken KE, Dougan M, Rose NR, Lichtman AH & Sharpe AH Adverse Events Following Cancer Immunotherapy: Obstacles and Opportunities. Trends Immunol 40, 511–523, doi:10.1016/j.it.2019.04.002 (2019). [PubMed: 31053497]

14. Burke KP, Grebinoski S, Sharpe AH & Vignali DAA Understanding adverse events of immunotherapy: A mechanistic perspective. Journal of Experimental Medicine 218, doi:10.1084/jem.20192179 (2020).
15. Gearty SV et al. An autoimmune stem-like CD8 T cell population drives type 1 diabetes. Nature, doi:10.1038/s41586-021-04248-x (2021).
16. Chen Y-G, Mathews CE & Driver JP The Role of NOD Mice in Type 1 Diabetes Research: Lessons from the Past and Recommendations for the Future. Frontiers in Endocrinology 9, doi:10.3389/fendo.2018.00051 (2018).
17. Christianson SW, Shultz LD & Leiter EH Adoptive transfer of diabetes into immunodeficient NOD-scid/scid mice. Relative contributions of CD4+ and CD8+ T-cells from diabetic versus prediabetic NOD.NON-Thy-1a donors. Diabetes 42, 44–55, doi:10.2337/diab.42.1.44 (1993). [PubMed: 8093606]
18. Varela-Calvino R, Calviño-Sampedro C, Gómez-Touriño I & Cordero OJ Apportioning Blame: Autoreactive CD4(+) and CD8(+) T Cells in Type 1 Diabetes. Arch Immunol Ther Exp (Warsz) 65, 275–284, doi:10.1007/s00005-016-0452-4 (2017). [PubMed: 28083620]
19. Yeo L et al. Autoreactive T effector memory differentiation mirrors β cell function in type 1 diabetes. J Clin Invest 128, 3460–3474, doi:10.1172/jci120555 (2018). [PubMed: 29851415]
20. Skowera A et al. β-cell-specific CD8 T cell phenotype in type 1 diabetes reflects chronic autoantigen exposure. Diabetes 64, 916–925, doi:10.2337/db14-0332 (2015). [PubMed: 25249579]
21. Abdelsamed HA et al. Beta cell-specific CD8(+) T cells maintain stem cell memory-associated epigenetic programs during type 1 diabetes. Nat Immunol 21, 578–587, doi:10.1038/s41590-020-0633-5 (2020). [PubMed: 32231298]
22. Zakharov PN, Hu H, Wan X & Unanue ER Single-cell RNA sequencing of murine islets shows high cellular complexity at all stages of autoimmune diabetes. J Exp Med 217, doi:10.1084/jem.20192362 (2020).
23. Bettini M et al. Cutting edge: accelerated autoimmune diabetes in the absence of LAG-3. J Immunol 187, 3493–3498, doi:10.4049/jimmunol.1100714 (2011). [PubMed: 21873518]
24. Kotecha N, Krutzik PO & Irish JM Web-based analysis and publication of flow cytometry experiments. Curr Protoc Cytom Chapter 10, Unit 10.17, doi:10.1002/0471142956.cy1017s53 (2010).
25. Zhang Q et al. LAG3 limits regulatory T cell proliferation and function in autoimmune diabetes. Sci Immunol 2, doi:10.1126/sciimmunol.aah4569 (2017).
26. Miller BC et al. Subsets of exhausted CD8(+) T cells differentially mediate tumor control and respond to checkpoint blockade. Nat Immunol 20, 326–336, doi:10.1038/s41590-019-0312-6 (2019). [PubMed: 30778252]
27. Chee J et al. Effector-Memory T Cells Develop in Islets and Report Islet Pathology in Type 1 Diabetes. The Journal of Immunology 192, 572–580, doi:10.4049/jimmunol.1302100 (2014). [PubMed: 24337380]
28. Kuric E et al. Demonstration of Tissue Resident Memory CD8 T Cells in Insulitic Lesions in Adult Patients with Recent-Onset Type 1 Diabetes. Am J Pathol 187, 581–588, doi:10.1016/j.ajpath.2016.11.002 (2017). [PubMed: 28212742]
29. Lennon GP et al. T cell islet accumulation in type 1 diabetes is a tightly regulated, cell-autonomous event. Immunity 31, 643–653, doi:10.1016/j.immuni.2009.07.008 (2009). [PubMed: 19818656]
30. Paley MA et al. Progenitor and terminal subsets of CD8+ T cells cooperate to contain chronic viral infection. Science 338, 1220–1225, doi:10.1126/science.1229620 (2012). [PubMed: 23197535]
31. Li J, He Y, Hao J, Ni L & Dong C High Levels of Eomes Promote Exhaustion of Anti-tumor CD8(+) T Cells. Front Immunol 9, 2981, doi:10.3389/fimmu.2018.02981 (2018). [PubMed: 30619337]
32. Seo W, Jerin C & Nishikawa H Transcriptional regulatory network for the establishment of CD8+ T cell exhaustion. Experimental & Molecular Medicine 53, 202–209, doi:10.1038/s12276-021-00568-0 (2021). [PubMed: 33627794]
33. Canale FP et al. CD39 Expression Defines Cell Exhaustion in Tumor-Infiltrating CD8(+) T Cells. Cancer Res 78, 115–128, doi:10.1158/0008-5472.Can-16-2684 (2018). [PubMed: 29066514]

34. Gupta PK et al. CD39 Expression Identifies Terminally Exhausted CD8+ T Cells. PLOS Pathogens 11, e1005177, doi:10.1371/journal.ppat.1005177 (2015). [PubMed: 26485519]
35. Bengsch B et al. Bioenergetic Insufficiencies Due to Metabolic Alterations Regulated by the Inhibitory Receptor PD-1 Are an Early Driver of CD8(+) T Cell Exhaustion. Immunity 45, 358–373, doi:10.1016/j.immuni.2016.07.008 (2016). [PubMed: 27496729]
36. Scharping NE et al. Mitochondrial stress induced by continuous stimulation under hypoxia rapidly drives T cell exhaustion. Nat Immunol 22, 205–215, doi:10.1038/s41590-020-00834-9 (2021). [PubMed: 33398183]
37. Scharping NE et al. The Tumor Microenvironment Represses T Cell Mitochondrial Biogenesis to Drive Intratumoral T Cell Metabolic Insufficiency and Dysfunction. Immunity 45, 701–703, doi:10.1016/j.immuni.2016.08.009 (2016). [PubMed: 27653602]
38. Sato Y et al. Cellular hypoxia of pancreatic beta-cells due to high levels of oxygen consumption for insulin secretion in vitro. J Biol Chem 286, 12524–12532, doi:10.1074/jbc.M110.194738 (2011). [PubMed: 21296882]
39. Olsson R, Olerud J, Pettersson U & Carlsson P-O Increased Numbers of Low-Oxygenated Pancreatic Islets After Intraportal Islet Transplantation. Diabetes 60, 2350–2353, doi:10.2337/db09-0490 (2011). [PubMed: 21788575]
40. Olsson R & Carlsson PO A low-oxygenated subpopulation of pancreatic islets constitutes a functional reserve of endocrine cells. Diabetes 60, 2068–2075, doi:10.2337/db09-0877 (2011). [PubMed: 21788581]
41. Komatsu H, Kandeel F & Mullen Y Impact of Oxygen on Pancreatic Islet Survival. Pancreas 47, 533–543, doi:10.1097/mpa.0000000000001050 (2018). [PubMed: 29621044]
42. Liao Y, Wang J, Jaehnig EJ, Shi Z & Zhang B WebGestalt 2019: gene set analysis toolkit with revamped UIs and APIs. Nucleic Acids Res 47, W199–w205, doi:10.1093/nar/gkz401 (2019). [PubMed: 31114916]
43. Huang da W, Sherman BT & Lempicki RA Bioinformatics enrichment tools: paths toward the comprehensive functional analysis of large gene lists. Nucleic Acids Res 37, 1–13, doi:10.1093/nar/gkn923 (2009). [PubMed: 19033363]
44. Kanehisa M Toward understanding the origin and evolution of cellular organisms. Protein Sci 28, 1947–1951, doi:10.1002/pro.3715 (2019). [PubMed: 31441146]
45. Kanehisa M & Goto S KEGG: Kyoto Encyclopedia of Genes and Genomes. Nucleic Acids Research 28, 27–30, doi:10.1093/nar/28.1.27 (2000). [PubMed: 10592173]
46. Kanehisa M, Sato Y, Furumichi M, Morishima K & Tanabe M New approach for understanding genome variations in KEGG. Nucleic Acids Res 47, D590–d595, doi:10.1093/nar/gky962 (2019). [PubMed: 30321428]
47. Priatel J, Huang Y-H, Tsai K, Harder K & Tan R SLAM-associated protein modulates CD8 T cell responses primed by antigen-presenting B cells (IRM4P.503). The Journal of Immunology 192, 61.10-61.10 (2014).
48. Creelan BC & Antonia SJ The NKG2A immune checkpoint — a new direction in cancer immunotherapy. Nature Reviews Clinical Oncology 16, 277–278, doi:10.1038/s41571-019-0182-8 (2019).
49. Trapnell C et al. The dynamics and regulators of cell fate decisions are revealed by pseudotemporal ordering of single cells. Nature Biotechnology 32, 381–386, doi:10.1038/nbt.2859 (2014).
50. Haghverdi L, Büttner M, Wolf FA, Buettner F & Theis FJ Diffusion pseudotime robustly reconstructs lineage branching. Nature Methods 13, 845–848, doi:10.1038/nmeth.3971 (2016). [PubMed: 27571553]
51. Das J & Yu H HINT: High-quality protein interactomes and their applications in understanding human disease. BMC Syst Biol 6, 92, doi:10.1186/1752-0509-6-92 (2012). [PubMed: 22846459]
52. Cusick ME et al. Literature-curated protein interaction datasets. Nat Methods 6, 39–46, doi:10.1038/nmeth.1284 (2009). [PubMed: 19116613]
53. Kent SC et al. Expanded T cells from pancreatic lymph nodes of type 1 diabetic subjects recognize an insulin epitope. Nature 435, 224–228, doi:10.1038/nature03625 (2005). [PubMed: 15889096]
54. Nakayama M et al. Prime role for an insulin epitope in the development of type 1 diabetes in NOD mice. Nature 435, 220–223, doi:10.1038/nature03523 (2005). [PubMed: 15889095]

55. Krishnamurthy B et al. Responses against islet antigens in NOD mice are prevented by tolerance to proinsulin but not IGRP. J Clin Invest 116, 3258–3265, doi:10.1172/jci29602 (2006). [PubMed: 17143333]

56. Prasad S, Xu D & Miller SD Tolerance strategies employing antigen-coupled apoptotic cells and carboxylated PLG nanoparticles for the treatment of type 1 diabetes. Rev Diabet Stud 9, 319–327, doi:10.1900/rds.2012.9.319 (2012). [PubMed: 23804269]

57. Amrani A et al. Progression of autoimmune diabetes driven by avidity maturation of a T-cell population. Nature 406, 739–742, doi:10.1038/35021081 (2000). [PubMed: 10963600]

58. Woo SR et al. Immune inhibitory molecules LAG-3 and PD-1 synergistically regulate T-cell function to promote tumoral immune escape. Cancer Res 72, 917–927, doi:10.1158/0008-5472.Can-11-1620 (2012). [PubMed: 22186141]

59. Andrews LP et al. Resistance to PD1 blockade in the absence of metalloprotease-mediated LAG3 shedding. Sci Immunol 5, doi:10.1126/sciimmunol.abc2728 (2020).

60. Blackburn SD et al. Coregulation of CD8+ T cell exhaustion by multiple inhibitory receptors during chronic viral infection. Nat Immunol 10, 29–37, doi:10.1038/ni.1679 (2009). [PubMed: 19043418]

61. Grebinoski S & Vignali DAA Inhibitory receptor agonists: the future of autoimmune disease therapeutics? Current Opinion in Immunology 67, 1–9, doi:10.1016/j.coi.2020.06.001 (2020). [PubMed: 32619929]

62. Jones BE et al. Fewer LAG-3+ T Cells in Relapsing-Remitting Multiple Sclerosis and Type 1 Diabetes. The Journal of Immunology, ji2100850, doi:10.4049/jimmunol.2100850 (2022).

Methods References

63. Godec J et al. Compendium of Immune Signatures Identifies Conserved and Species-Specific Biology in Response to Inflammation. Immunity 44, 194–206, doi:10.1016/j.immuni.2015.12.006 (2016). [PubMed: 26795250]

64. Pauken KE et al. Epigenetic stability of exhausted T cells limits durability of reinvigoration by PD-1 blockade. Science 354, 1160–1165, doi:10.1126/science.aaf2807 (2016). [PubMed: 27789795]

65. Doering TA et al. Network analysis reveals centrally connected genes and pathways involved in CD8+ T cell exhaustion versus memory. Immunity 37, 1130–1144, doi:10.1016/j.immuni.2012.08.021 (2012). [PubMed: 23159438]

66. Leiter EH The NOD mouse: a model for insulin-dependent diabetes mellitus. Curr Protoc Immunol Chapter 15, Unit 15.19, doi:10.1002/0471142735.im1509s24 (2001).

67. Rodriguez-Calvo T, Ekwall O, Amirian N, Zapardiel-Gonzalo J & von Herrath MG Increased immune cell infiltration of the exocrine pancreas: a possible contribution to the pathogenesis of type 1 diabetes. Diabetes 63, 3880–3890, doi:10.2337/db14-0549 (2014). [PubMed: 24947367]

68. Watson MJ et al. Metabolic support of tumour-infiltrating regulatory T cells by lactic acid. Nature 591, 645–651, doi:10.1038/s41586-020-03045-2 (2021). [PubMed: 33589820]

69. Roederer M, Nozzi JL & Nason MC SPICE: exploration and analysis of post-cytometric complex multivariate datasets. Cytometry A 79, 167–174, doi:10.1002/cyto.a.21015 (2011). [PubMed: 21265010]

70. Picelli S et al. Smart-seq2 for sensitive full-length transcriptome profiling in single cells. Nat Methods 10, 1096–1098, doi:10.1038/nmeth.2639 (2013). [PubMed: 24056875]

71. Dobin A et al. STAR: ultrafast universal RNA-seq aligner. Bioinformatics 29, 15–21, doi:10.1093/bioinformatics/bts635 (2013). [PubMed: 23104886]

72. Law CW, Chen Y, Shi W & Smyth GK voom: Precision weights unlock linear model analysis tools for RNA-seq read counts. Genome Biol 15, R29, doi:10.1186/gb-2014-15-2-r29 (2014). [PubMed: 24485249]

73. Ritchie ME et al. limma powers differential expression analyses for RNA-sequencing and microarray studies. Nucleic Acids Res 43, e47, doi:10.1093/nar/gkv007 (2015). [PubMed: 25605792]

74. Smyth GK Linear models and empirical bayes methods for assessing differential expression in microarray experiments. Stat Appl Genet Mol Biol 3, Article3, doi:10.2202/1544-6115.1027 (2004). [PubMed: 16646809]

75. Mootha VK et al. PGC-1alpha-responsive genes involved in oxidative phosphorylation are coordinately downregulated in human diabetes. Nat Genet 34, 267–273, doi:10.1038/ng1180 (2003). [PubMed: 12808457]

76. Subramanian A et al. Gene set enrichment analysis: a knowledge-based approach for interpreting genome-wide expression profiles. Proc Natl Acad Sci U S A 102, 15545–15550, doi:10.1073/pnas.0506580102 (2005). [PubMed: 16199517]

77. Stoeckius M et al. Cell Hashing with barcoded antibodies enables multiplexing and doublet detection for single cell genomics. Genome Biology 19, 224, doi:10.1186/s13059-018-1603-1 (2018). [PubMed: 30567574]

78. Stuart T et al. Comprehensive Integration of Single-Cell Data. Cell 177, 1888–1902.e1821, doi:10.1016/j.cell.2019.05.031 (2019). [PubMed: 31178118]

79. Cillo AR et al. Immune Landscape of Viral- and Carcinogen-Driven Head and Neck Cancer. Immunity 52, 183–199.e189, doi:10.1016/j.immuni.2019.11.014 (2020). [PubMed: 31924475]

80. Becht E et al. Dimensionality reduction for visualizing single-cell data using UMAP. Nature Biotechnology 37, 38–44, doi:10.1038/nbt.4314 (2019).

81. Wickham H ggplot2; Elegant Graphics for Data Analysis. Springer-Verlag (2009).

82. Wickham H et al. Welcome to the Tidyverse. The Journal of open Source Software 4, 1686, doi:10.21105/joss.01686 (2019).

83. Shannon P et al. Cytoscape: a software environment for integrated models of biomolecular interaction networks. Genome Res 13, 2498–2504, doi:10.1101/gr.1239303 (2003). [PubMed: 14597658]

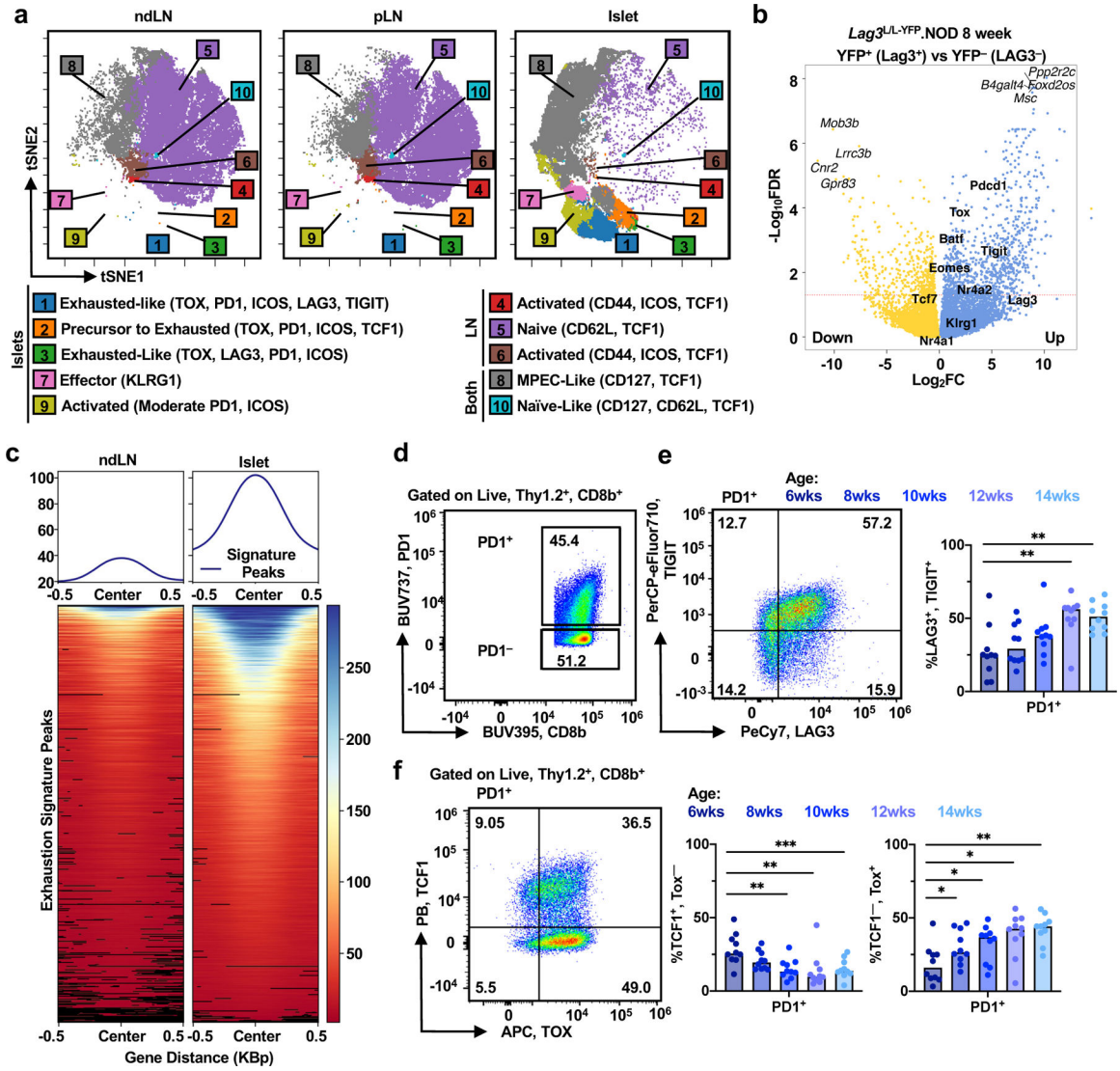

Figure 1: Intra-Islet CD8$^+$ T cells feature hallmarks of exhaustion.

The phenotype of intra-islet CD8$^+$ T cells was assessed by high-dimensional spectral flow cytometry, bulk RNAseq and scATACseq. (a) High dimensional analysis of spectral flow cytometry data of 11 markers on CD8$^+$ T cells from the islets of 12-week-old female NOD using Cytobank (Methods)[24]. ViSNE maps were fed into FlowSOM clustering algorithm. (b) Bulk population RNAseq comparing intra-islet YFP$^+$ and YFP$^-$ CD8$^+$ T cells, along with ndLN and pLN as controls. Cells were pooled from 3 *Lag3*$^{L/L\text{-}YFP}$.NOD 8-week-old females in 2 independent experiments. Volcano plot illustrating top 4 differentially expressed genes (up and down) in non-bold, as well as markers of exhaustion in bold. (c) scATACseq comparing CD8$^+$ T cells from the islets or ndLN of 8-week-old E8i$^{CRE/CRE\text{-}GFP}$.NOD female mice (n = 4). Enrichment for exhaustion signature peaks is shown. (d) Representative flow cytometry plot of PD1 expression on intra-islet CD8$^+$ T cells gated on Live, Thy1.2$^+$, CD8b$^+$, PD1$^+$. (e) Quantification of LAG3 and TIGIT expression on PD1$^+$ cells over time (6 vs 12, 14 p=.0065, .0039). (f) Representative flow plot and quantification of TCF1 and TOX staining on Live, Thy1.2$^+$, CD8b$^+$, PD1$^+$. Gating based on total or PD1$^-$ CD8$^+$ T cells

(Extended Data Fig. 1e, 4c–d). (6 vs 10, 12, 14 p=.0027, .0019, .0064). (a, d-f) Spectral flow cytometry for $CD8^+$ T cell functional markers was completed over a time course of 6–14 week old female WT NOD mice. Representative flow plots are derived from intra-islet $CD8^+$ T cells (gated on lymphocytes, single cells, Live, $Thy1.2^+$, $CD8b^+$) of 12-week-old female NOD. Data were accumulated from a total of 5 experiments, each experiment had mice of several ages with n = 10 mice per timepoint, n = 50 total mice. Each point on the graph is representative of a single mouse. A two-sided nonparametric Mann-Whitney was preformed, where P = * <0.05, ** < 0.01, *** < 0.001, **** < 0.0001. Graphs portray the median. Unlabeled indicates not statistically significant.

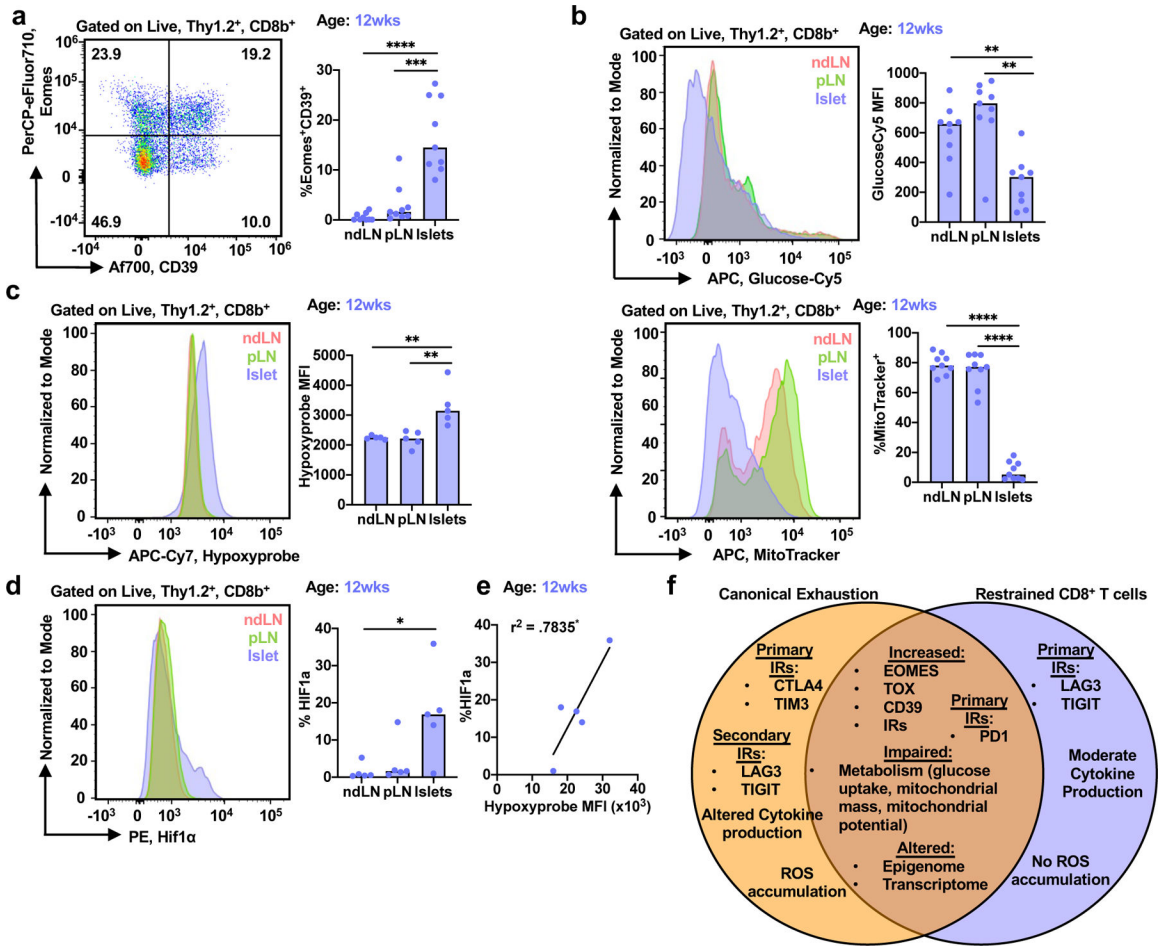

Figure 2: Intra-islet CD8$^+$ T cells are different from canonically exhausted CD8$^+$ cells

(a-e) Flow cytometric analysis of intra-islet CD8$^+$ T cells from 12-week-old female WT NODs. (a) Representative flow gating and quantification of Eomes and CD39 expression (Islets vs ndLN, pLN p= <.0001, .0005), (b) GlucoseCy5 (Islets vs ndLN, pLN p= .0027, .0012) and MitoTracker (Islets vs ndLN and pLN p= <.0001), (c) Hypoxyprobe (Islets vs. ndLN, pLN, p=.0079, .00709), (d) Hif1α (Islets vs. ndLN, p=.0159) and (e) correlation between correlation of Hypoxyprobe to MFI to HIF1α (p=.0459). (f) Diagram comparing canonical exhaustion to what we observe in the islets. (a-b) Data is representative of 2 experiments, with n = 10. (c-d) Data is representative of 1 experiment with n=5 WT NODs. (a-e) Each point on the graph represents 1 mouse. A two-sided nonparametric Mann-Whitney test was performed. Graphs portray the median. (d) Pearson's correlation coefficients and r^2 values were calculated. (a-e) P = * <0.05, ** < 0.01, *** < 0.001, **** < 0.0001. Unlabeled indicates not statistically significant.

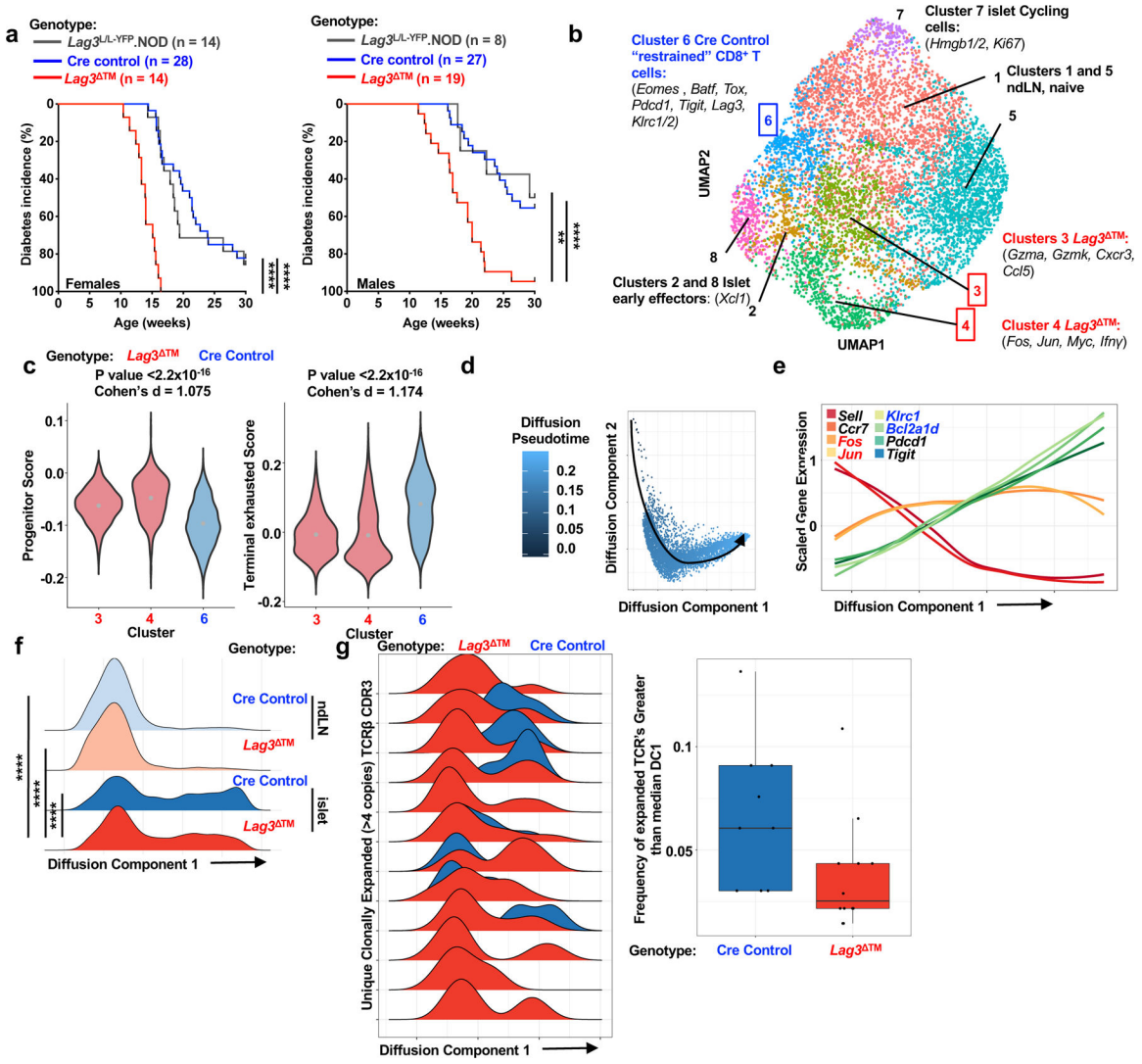

Figure 3: LAG3 deletion accelerates disease and halts development in a progenitor stage.

(a) Diabetes incidence in female and male Cre Control (n=28 females, 27 males), *Lag3*$^{L/L\text{-}YFP}$.NOD (n=14 females, 8 males) and *Lag3*$^{\Delta TM}$.NOD (n=14 females, 19 males). A log-rank (Mantel-Cox) test was used to compare survival curves. (Females: *Lag3*$^{\Delta TM}$ vs. *Lag3*$^{L/L\text{-}YFP}$.NOD, Cre Control, p<.0001 for both comparisons. Males: *Lag3*$^{\Delta TM}$ vs. *Lag3*$^{L/L\text{-}YFP}$.NOD, Cre Control, p=.0042, <.0001) (b-g) CD8^{+} T cells from the islets and ndLN were isolated from 4 Cre Control and 4 *Lag3*$^{\Delta TM}$ 8-week-old female NOD mice and were subjected to paired 5' scRNAseq and scTCRseq. (b) Cells were visualized by UMAP, and clustering was performed using DRAGON (Methods). Red is representative of *Lag3*$^{\Delta TM}$ dominated islet clusters, 3 and 4. Blue is representative of Cre Control dominated islet cluster, 6. Selected functional genes from the top 50 DEGs in each cluster are annotated (Supplementary Table 2). (c) Gene set enrichment analysis using progenitor and terminal exhausted gene sets[26] (Methods). A two-sided T test was used to compare *Lag3*$^{\Delta TM}$ versus Cre Control, the median point is shown on the graph. (d) Diffusion pseudotime analysis was preformed using Destiny (Methods), where cells are embedded in diffusion space using the

first two diffusion components DC1 and DC2. (e) Scaled gene expression of selected genes as a function of increasing pseudotime along DC1. Red lettering corresponds to markers of *Lag3*$^{\Delta TM}$ dominated clusters and blue lettering is representative of Cre Control dominated cluster markers by ORA. (f) Cell density along DC1. A two-sided Kolmogorov-Smirnov test assess distributions along DC1 (Islet *Lag3*$^{\Delta TM}$ vs Islet Cre Control, ndLN *Lag3*$^{\Delta TM}$, ndLN Cre Control, p=1.522x10^{-9}, <2.22x10^{-16}, <2.22x10^{-16}). (g) Comparison of clonally expanded TCRs (greater than 4 copies) across DC1 comparing Cre Control versus *Lag3*$^{\Delta TM}$ within the islets. A box and whisker plot shows frequency of TCRs in greater than median DC1 in each genotype. Here, the line is the median, box is lower and upper quantiles (lower 25% and upper 25%), the upper whisker is the minimum of either the maximum value or the upper quartile plus 1.5 times the interquartile ranger. Bottom whisker is the maximum of the minimum or the first quartile minus 1.5 times in interquartile ranger. A two-sided Wilcoxon rank sum test was used (p=0.024). (a-g) P = * <0.05, ** < 0.01, *** < 0.001, **** < 0.0001.

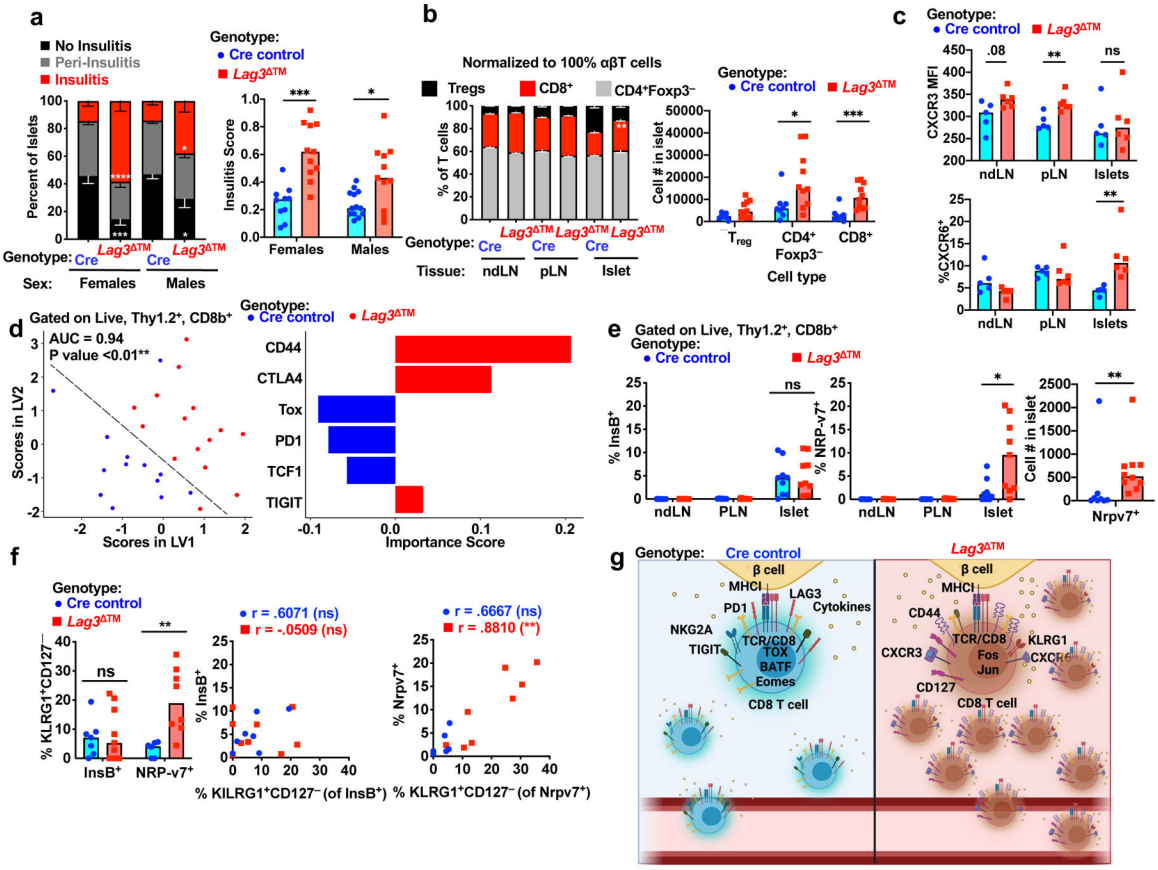

Figure 4: LAG3 deletion accelerates disease by perturbing the ‘restrained’ phenotype.

(a) Insulitis and scoring of 8-week-old female and male Cre Controls (10 females, 13 males) and *Lag3*$^{\Delta TM}$ NOD mice (11 females, 11 males) (insulitis: Female Cre Control vs *Lag3*$^{\Delta TM}$ no insulitis, peri insulitis, insulitis, p = .0006, .05, <.0001, Male Cre Control vs *Lag3*$^{\Delta TM}$ no insulitis, peri insulitis, insulitis, p=.0257, .1139, .00218, Scoring: females p=.0001, males p=.0265). (b-f) Flow cytometry was performed on 8-week-old female *Lag3*$^{\Delta TM}$ and Cre Controls taking cells from ndLN, pLN and islets. (b) Quantification of T cell percentages and numbers (Percent CD8’s comparing Cre Control vs *Lag3*$^{\Delta TM}$ islets p=.0058, Cell numbers CD4^{+}Foxp3^{-}, CD8^{+} p=.028, .0009). Data is representative of 3 independent experiments with n=8–10 per genotype. (c) Chemokine receptor expression with data representative of 2 independent experiment with n=5–6 per genotype (CXCR3 ndLN, pLN, Islet p=.08, .0065, .9, CXCR6 Islet p=.0043). (d) Partial least squares-discriminant analysis (PLS-DA) of exhaustion/activation markers assessed by flow cytometry with data representative of 3 independent experiments n=13–15 per genotype. For the binary classification by genotype AUC = 0.94 in a k-fold cross-validation framework, P < 0.01 compared to a negative control model built using permuted label. (e) Quantification of percent tetramer^{+} CD8^{+} T cells found in the islets with data representative of 3 independent experiments with n = 9 per genotype (%InsB^{+}, Nrpv7^{+} p=.8, .01, #Nrpv7^{+} p=.0061). (f) Quantification of tetramer^{+} SLECs (p=.003) and correlation of percent tetramer^{+} to percent SLECS with data representative of 3 independent experiments with n = 8–10 per genotype (%InsB correlation to SLECs Cre Control, *Lag3*$^{\Delta TM}$ p=.08, .9, %Nrpv7

correlation to SLECs Cre Control, *Lag3*$^{\Delta TM}$ p=.22, .0027). Graphs show only samples having >100 Tetramer^{+} cells. Correlation calculation was preformed using Pearson's correlation coefficients and r^2 values were calculated. (g) Model depicting the consequences of LAG3 deletion on CD8^{+} T cells in islets. Created with BioRender.com. (a-f) A two-sided nonparametric Mann-Whitney test for significance was preformed (unless otherwise noted). Each data point corresponds to a single mouse. Graphs portray the median and error bars are the SEM. P = * <0.05, ** < 0.01, *** < 0.001, **** < 0.0001. Unlabeled indicates not statistically significant.